Rare Met. (2021) 40(2):448–470
https://doi.org/10.1007/s12598-020-01649-1

RARE METALS
www.editorialmanager.com/rmet

REVIEW

Recent advances and perspective in metal coordination materials-based electrode materials for potassium-ion batteries

**Fei Wang, Yong Liu*, Hui-Jie Wei, Teng-Fei Li, Xun-Hui Xiong,
Shi-Zhong Wei, Feng-Zhang Ren*, Alex A. Volinsky**

Received: 2 July 2020 / Revised: 20 October 2020 / Accepted: 3 November 2020 / Published online: 7 January 2021

Abstract Recently, to ameliorate the forthcoming energy crisis, sustainable energy conversion and storage devices have been extensively investigated. Potassium-ion batteries (KIBs) have aroused widespread attention in these very active research applications due to their earth abundance and similar low redox potential compared to Li-ion batteries (LIBs). It is critical to develop electrode materials with large ion diffusion channels and robust structures for long cycling performance in KIBs. Metal coordination materials, including metal–organic frameworks, Prussian blue, and Prussian blue analogue, as well as their composites and derivatives, are known as promising materials for high-performance KIBs due to their open frameworks, large interstitial voids, functionality and tailorability. In this review, we give an overview of the recent advances on the application of metal coordination materials in KIBs. In addition, the methods to enhance their K-ion storage properties are summarized and discussed, such as morphology engineering, doping, as well as compositing with other materials. Ultimately, some prospects for future research of metal coordination materials for KIBs are also proposed.

Keywords Metal–organic frameworks; Prussian blue; Prussian blue analogue; Composites; Derivatives; Potassium-ion batteries

1 Introduction

With growing demands for renewable energy utilization and environment protection in a developing modern society, significant efforts have been devoted to exploiting electric energy conversion and storage devices to maximize the utilization of intermittent renewable solar and wind energy [1–6]. Among these electrical energy storage devices, lithium-ion batteries (LIBs), with high energy density, long cycle life, and environmentally benign profile, have been widely applied in portable electronics, electrical vehicles, and smart grids [7–13]. However, limited lithium resources in the earth's crust and the associated high cost hinder further large-scale applications of LIBs [14–20]. However, with physicochemical properties similar to those of Li, sodium and potassium present abundant resources in nature. Hence, sodium-ion batteries (SIBs) and potassium-ion batteries (KIBs) are extensively investigated

---

F. Wang, Y. Liu*, H.-J. Wei, T.-F. Li, F.-Z. Ren*
Provincial and Ministerial Co-construction of Collaborative Innovation Center for Non-ferrous Metal New Materials and Advanced Processing Technology, Henan Key Laboratory of Non-Ferrous Materials Science and Processing Technology, School of Materials Science and Engineering, Henan University of Science and Technology, Luoyang 471023, China
e-mail: liuyong209@haust.edu.cn

F.-Z. Ren
e-mail: renfz@haust.edu.cn

Y. Liu, S.-Z. Wei
National Joint Engineering Research Center for Abrasion Control and Molding of Metal Materials, Henan Key Laboratory of High-Temperature Structural and Functional Materials, Henan University of Science and Technology, Luoyang 471003, China

X.-H. Xiong
Guangzhou Key Laboratory of Surface Chemistry of Energy Materials, New Energy Research Institute, School of Environment and Energy, South China University of Technology, Guangzhou 510006, China

A. A. Volinsky
Department of Mechanical Engineering, University of South Florida, Tampa, FL 33620, USA

[21–26]. In addition, in comparison to the standard electrode potentials of Na^+/Na (– 2.71 V vs. standard hydrogen electrode (SHE)), the standard potential of K^+/K (– 2.93 V vs. SHE) is close to that of Li^+/Li (– 2.79 V vs. SHE) [23, 27], which indicates that KIBs present potential high energy density for applications. Unfortunately, K-ions show depressed diffusion kinetics in typical materials of LIBs and SIBs, which are attributed to the large ionic radius of the K-ion (0.138 nm) relative to that of the Li-ion (0.076 nm) or the Na ion (0.102 nm) [28]. Therefore, exploiting advanced materials with large ion channels and designing appropriate electrode structures with excellent structural integrity for KIBs are urgent actions to pursue.

Metal coordination materials, including metal–organic frameworks (MOFs) and Prussian blue (PB), are mainly composed of metal nodes and organic linkers [29–31]. These metal nodes consist of elements of alkaline earth metals or transition metals, and the organic linkers are normally N-donor groups, carboxylates, or even phosphonates [32–36]. The comparison of the advantages and disadvantages of MOF and PB is shown in Fig. 1. MOFs and PB could offer large interstitial spaces and robust structures for K^+ (de)insertion. In addition, due to facile synthesis and economical raw materials, MOF and PB are potential electrode materials for KIBs. An MOF with abundant electroactive constituents can provide abundant active sites. However, MOF materials usually have high cost and poor conductivity. As for PB materials, those containing K-ions can be used as cathode materials in KIBs and provide high voltage plateaus. Nevertheless, due to the rapid synthetic process of PB, there are vacancies and crystal water in the product, which have a negative effect on coulombic efficiency. In recent years, many research efforts have been applied to the development of the electrochemical performance of MOF and PB materials in KIBs. Nevertheless, the poor electronic conductivity and chemical instability of those materials hinder their further application. In this regard, MOFs and PB composites and derivations could present excellent conductivity, large surface areas, adjustable pore sizes, and abundant active sites, enhancing their K^+ storage properties. For instance, Liu et al. [37] synthesized N-doped hollow carbon-onion-constructed nanosheets (HCONs) derived from MOFs, which demonstrated abundant active sites and improved ion diffusions. MOFs and PB-based materials have received considerable attention in recent years (Fig. 2a, b), and there has been a gradual increase in publications of studies of metal coordination materials in KIBs (Fig. 2c). Furthermore, Zhou et al. [30] recently reviewed a comprehensive introduction on advanced applications of HCFs (the mainstream PBA cathodes) in SIBs and KIBs. However, a crucial review that focuses exclusively on metal coordination materials for KIBs has rarely been reported.

Herein, we provide an overview of metal coordination materials, mainly including metal–organic frameworks, Prussian blue, and Prussian blue analogue, as well as their composites and derivatives, and their applications as electrode materials for KIBs. Their micro/nanostructures and electrochemical properties are systematically summarized. Furthermore, some reasonable suggestions to promote future breakthroughs are also presented.

2 Metal–organic framework (MOF)

MOFs are potential electrode materials in KIBs due to their abundant reactive sites and large ion diffusion channels. In addition, through the pyrolysis of MOFs and subsequent etching away of metal, MOF-derived carbon materials usually possess a porous structure and a high specific

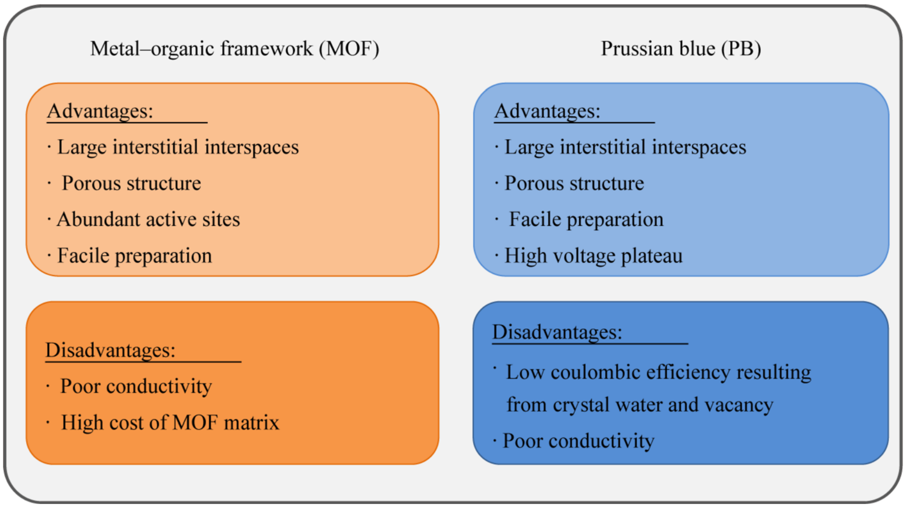

Fig. 1 Comparison of advantages and disadvantages of metal–organic framework (MOF) and Prussian blue (PB) materials in KIBs

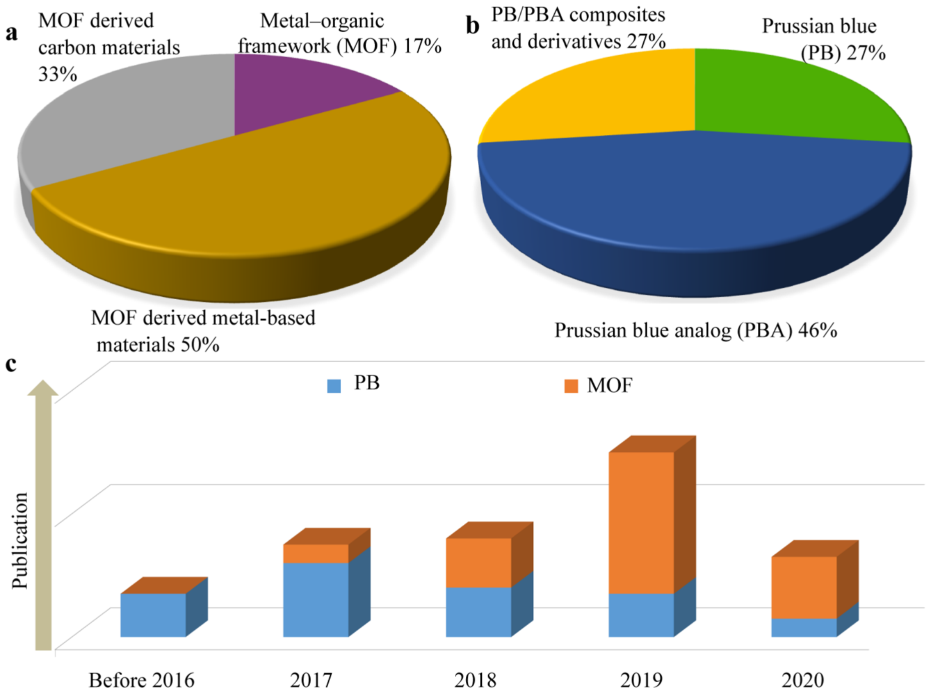

Fig. 2 **a** Pie chart of ratio of different categories of MOFs materials for potassium-ion batteries (KIBs); **b** pie chart of ratio of different categories of PB materials for KIBs; **c** bar chart of research trend of MOF and PB materials in KIBs

surface area. In addition, heteroatoms in organic ligands of MOFs can regulate the electronic structure and increase the adsorption energy of K-ions. For example, ZIF-67 derived carbon materials with higher nitrogen content (indicating more abundant defects) exhibit better K-storage performance than those with lower nitrogen content [38]. Furthermore, through the heat treatment of MOFs in a reducing atmosphere (e.g., phosphorus, sulfur, or selenium), a series of MOF-derived metal-based materials can be synthesized. These materials, with the alloying reaction and conversion reaction mechanisms in KIBs, can deliver high capacities. Therefore, by carefully designing structures and introducing high capacity materials, the electrochemical properties of electrode materials could be effectively improved. The electrochemical performances of these materials in KIBs are summarized in Table 1 [32–63].

2.1 Pristine MOF and its composites

MOFs, with large ion diffusion channels, abundant reactive constituents, and facile synthetic methods, are potential anodes in KIBs. For instance, Li et al. [32] explored cobalt(II) terephthalate-based MOF materials synthesized via a solvothermal approach as an anode electrode for KIBs, which delivered a charge capacity of 188 $mAh\cdot g^{-1}$ at 1 $A\cdot g^{-1}$ over 600 cycles. Through characterizations, the results demonstrated the reversible recovery of CoO/Co and the hybridized state of O 2p/Co 3d in an organic linker during discharge/charge, implying that Co units and oxygen-containing organic ligands were used for ion storage, and that the coordination of cobalt and oxygen were crucial for the reversibility of discharge and charge processes. The report shows that the capacity was related to center metal ions. In addition, An et al. [33] reported a MOF MIL-125(Ti) (MIL is material from Institute Lavoisier) as an anode in KIBs for the first time. It can maintain a 90.2% capacity retention over 2000 cycles at 0.2 $A\cdot g^{-1}$. The excellent capacity retention could be attributed to the ability to reversibly (de)insert K-ions into the organic moiety. To directly investigate the redox reaction of the organic ligand in KIBs, Li et al. [34] reported a novel K-MOF ($[C_7H_3KNO_4]_n$), developed from the organic ligand pyridine-2,6-dicarboxylic acid (H_2PDA) and K^+, which showed high performance due to the stable bonds of N–K and O–K in the K-MOF.

Phosphate organic linkers for MOF and iron-based MOF composites in KIBs were reported, respectively. Liao et al. [35] prepared $K_2[(VO)_2(HPO_4)_2(C_2O_4)]$ (K_2VPC) with platelet-like particle morphologies as a cathode material for KIBs. Through increasing the concentration of the precursor, small-sized (K_2VPC) $K_2[(VO)_2(HPO_4)_2(C_2O_4)]$ can be obtained. Based on incomplete potassiation and depotassiation during cycling ($K_2VPC - xe^- \leftrightarrow K_{2-x}VPC + xK^+$), K_2VPC exhibited 54 $mAh\cdot g^{-1}$ at 21.8 $mA\cdot g^{-1}$ over 200 cycles in a range of 2.0–4.6 V in

Table 1 Electrochemical performances of pristine metal–organic framework (MOF), and MOF derivatives in KIBs

Samples	Voltage window/V	ICE/%	Cyclability/CD/cycles/ ($mAh\cdot g^{-1}/mA\cdot g^{-1}$)	RC/CD/ ($mAh\cdot g^{-1}/mA\cdot g^{-1}$)	Refs.
Pristine MOF					
L-$Co_2(OH)_2$BDC	0.2–3	60.65	214/200/200	~ 131/1000	[32]
MIL-125(Ti)	0.01–3	58.86	157/50/200	56/200	[33]
K-MOF ($[C_7H_3KNO_4]_n$)	0.1–2	~ 25	123/50/150	44/500	[34]
$K_2[(VO)_2(HPO_4)_2(C_2O_4)]$	2–4.6	–	54/~ 22/200	<50/109	[35]
MOF-235/MCNTs	0.01–3	29.1	144/50/50	47/400	[36]
MOF derivatives					
HCONs	0.01–2.8	35.2	132/2000/5000	168/2000	[37]
High pyridine NPC	0.1–3	–	231.6/500/2000	186.2/2000	[38]
N-doped carbon nanotubes	0.01–3	24.45	102/2000/500	102/2000	[39]
CNT@PC	0.001–3	25.2	141/1000/1000	168/1000	[40]
AC@GC	0.01–3	15.7	137/1000/1500	170/2000	[41]
Cellular NC	0.01–3	–	218.5/300/600	123.2/2000	[42]
3D carbon networks	0.001–3	45	190/50/500	100/2000	[43]
3D NPC	0.01–3	–	292/100/400	94/10,000	[44]
NSC-microboxes	0.1–3	–	180.5/500/1000	155.6/2000	[45]
OFPC nanopolyhedra	0.01–3	27	218/1000/2000	171/2000	[46]
NOMC octahedrons	0.001–3	~ 20	100/1000/1300	110/1000	[47]
ZNP/C-600	0.01–3	–	145/500/300	46/2000	[48]
UCF@CNs@BiN	0.01–3	–	327/100/600	140/1000	[49]
Sb-NPs@PC	0.01–2.6	69.7	497/100/100	160/2000	[50]
AC@CoP/NCNTs/CNFs	0.01–3	53.2	358.8/100/200	~ 292/3200	[51]
NC@CoP/NC	0.01–2.5	–	110/500/800	200/2000	[52]
FeP@C	0.01–3	–	163/200/100	–	[53]
3DG/FeP	0.01–3	–	327/100/100	127/2000	[54]
AC@CoS/NCNTs/CoS@CNF	0.01–3	57.6	401.2/100/100	166.8/3200	[55]
ZIF-67-C@MoS_2	0.01–3	66.5	199.8/100/50	60.5/2000	[56]
Co_9S_8/NSC@MoS_2@NSC	0.01–2.6	65.9	367/200/300	221/2000	[57]
Co_9S_8/N–C@MoS_2 DHNCs	0.01–3	89.1	< 80/1000/100	< 80/1000	[58]
FeS_2@RGO	0.01–3	55.3	123/500/420	151/500	[59]
$Co_{0.85}Se$@NC	0.01–3	57.9/	114.7/1000/250	110.7/2000	[60]
$Co_{0.85}Se$@CNFs	0.01–2.6	50.2	299/1000/400	303/2000	[61]
ZnSe@NDPC	0.01–3	41.1	262.8/100/200	109.4/2000	[62]
ZnSe–$FeSe_2$/RGO	0.01–3	77	363/50/100	–	[63]

ICE: initial coulombic efficiency, CD: current density, RC: rate capability, BDC: 1,4-benzenedicarboxylate, CNT: carbon nanotube, PC: porous carbon, AC: amorphous carbon, GC: graphitized carbon, HCONs: N-rich hollow carbon-onion-constructed nanosheets, NC: N-doped carbon, NPC: N-doped porous carbon, NSC: N/S codoped carbon, OFPC: O/F dual-doped porous carbon, ZNP: Zn nanoparticle, UCF@CNs@BiN: ultrathin carbon film@carbon nanorods@Bi nanoparticle, CNF: carbon nanofibers, ZIF: zeolite imidazole framework, DHNCs: dodecahedral heterogeneous nanocages, RGO: reduced grapheme oxide, NDPC: N-doped porous carbon, NOMC: N/O co-doped mesoporous carbon, 3DG: three-dimensional grapheme, MOF: metal organic framework, MCNTs: multiwalled carbon nanotubes, Sb-NPs@PC: Sb nanoparticles@porous carbon

KIBs. In addition, Deng et al. [36] proposed and prepared an economical iron-based MOF-235/multiwall-carbon tubes (MCNT) composite material, where its organic moiety can obtain/lose two electrons during the discharge/charge process, and the inactive iron ions ensure the structure stability. When tested in KIBs, the prepared composite could exhibit 132 $mAh\cdot g^{-1}$ at 0.2 $A\cdot g^{-1}$ after 200 cycles.

Based on the above studies on MOF and its composite in KIBs, the organic linkers provide ion diffusion channels and participate in K^+ storage. In addition, in MOF materials, active metal centers (for example, Co ions) could also play an important role in K^+ storage; some inactive metal centers (Fe) can ensure the structure stability during cycles. Therefore, due to an abundance of their precursor materials, MOF materials are deemed as potential cathode and anode electrode materials for KIBs.

2.2 Derivatives

Although pristine MOF materials exhibit favorable K-storage properties, to further develop electrode materials for KIBs, MOF-based derivatives, such as MOF-derived carbon- and metal-based materials, have been extensively investigated. Carbon materials are usually prepared through the pyrolysis of MOF in an inert atmosphere and the subsequent etching away of metal centers. Derived carbon materials usually present a large specific surface area, rich active sites, and a conductive pathway for K-ion storage. MOF-derived metal-based materials are prepared using a process similar to the one used for the fabrication of MOF-derived carbon materials, except for the etching away of metal centers. As a result, metal or metallic compound particles are uniformly dispersed in carbon frameworks.

2.2.1 *MOF-derived carbon materials*

MOF-derived carbon materials are potential candidates for KIB electrodes due to their excellent conductivity and eco-friendliness. As research investigations progress, a variety of dimensional carbon materials are designed, such as carbon nanotubes, carbon nanosheets, and three-dimensional (3D) carbon networks. To further improve rate capability and cyclability, heteroatom-doped carbon materials are also exploited.

Nanostructure tubes with a large specific surface area and short diffusion path can present excellent kinetics and enhanced rate capability. In this regard, Xiong et al. [39] prepared nitrogen-doped carbon nanotubes (NCNTs) through the calcination of ZIF-67 under a reducing atmosphere followed by an etch with acid. The prepared process is shown in Fig. 3a. The reducing atmosphere enhances the induced effects of Co for the formation of carbon nanotubes. After heat treatment, ZIF-67 nanoparticles are derived into interconnected NCNTs, as shown in the scanning electron microscopy (SEM) image (Fig. 3c). The transmission electron microscopy (TEM) image (Fig. 3d) demonstrates that NCNTs show a hollow structure with an ~ 20-nm outer diameter. Moreover, the nitrogen adsorption–desorption isotherms (Fig. 3g) demonstrate that the NCNTs possess a high specific surface area of 126 $m^2 \cdot g^{-1}$. When used as anodes in KIBs (Fig. 3h), the NCNTs present a superior capacity of 180 $mAh \cdot g^{-1}$ at 0.5 $A \cdot g^{-1}$ and maintain 102 $mAh \cdot g^{-1}$ at 2 $A \cdot g^{-1}$. In addition, ex situ high-resolution transmission electron microscopy (HRTEM) and ex situ Raman spectroscopy of the NCNTs at different voltage states were carried out. Those results demonstrated that the graphite structure was maintained and the degree of graphitization was enhanced, which indicated the reversible insertion/extraction of K-ions in NCNTs. In addition, the ex situ HRTEM and ex situ Raman spectroscopy showed a reversible interlayer distance and a G-band shift during the full potassiation/depotassiation states, respectively, revealing the storage mechanism of reversible insertion/extraction of potassium ions in the NCNTs. Recently, Lu et al. [40] combined the advantages of carbon nanotubes and porous carbon to synthesize N-doped CNT-coated porous carbon (CNT@PC) through carbonization and treatment in a 1 $mol \cdot L^{-1}$ $FeCl_3$ solution of the MOF. The ex situ X-ray diffraction (XRD) analysis showed the KC_{24}/KC_8 phases and the distinct (002) diffraction peak at 0.001 V, which confirmed the intercalation and adsorption potassium storage mechanism for CNT@PC in KIBs, respectively. Finally, the carbon product delivered a specific capacity of 339 $mAh \cdot g^{-1}$ at 0.05 $A \cdot g^{-1}$ in KIBs.

Compared with one-dimensional (1D) materials, two-dimensional (2D) materials can exhibit better mechanical performance and a greater volume of designed space. For example, Li et al. [41] combined graphite carbon and amorphous carbon to design core–shell carbon nanoplates through carbonizing MOF nanoplates composed of a Zn-MOF core and a Co-MOF shell. The synthetic process is shown in Fig. 3b. The 2D carbon nanoplates (denoted as AC@GC) possess not only a graphitic carbon core with superior conductivity and low voltage plateaus, but an amorphous carbon shell as well, with a high nitrogen content, greater interlayer spacing, and more defect sites. The nanoporous AC@GC nanoplates (Fig. 3e) exhibit a porous, bumpy surface following the carbonization of Co-MOF, which indicates a prepared AC@GC with a core–shell structure. Moreover, TEM image (Fig. 3f) of AC@GC shows macropore and mesopore structures resulting from Co nanoparticles dissolution during etching. The Raman spectroscopy (Fig. 3i) further demonstrates the successful preparation of AC@GC. In addition, in situ Raman analysis demonstrated a higher degree of graphitization of AC@GC after depotassiation than the original one, which was attributed to the ability of potassium ions to occupy the defect sites during potassium insertion/desertion. When applied as an electrode in KIBs (Fig. 3j), the AC@GC electrode shows 310 $mAh \cdot g^{-1}$ at 0.1 $A \cdot g^{-1}$ after 200 cycles.

Similarly, to combine the advantages of amorphous carbon and graphitic carbon, Liu et al. [37] synthesized N-doped hollow carbon-onion-constructed nanosheets (HCONs) derived from co-hexamine materials. The

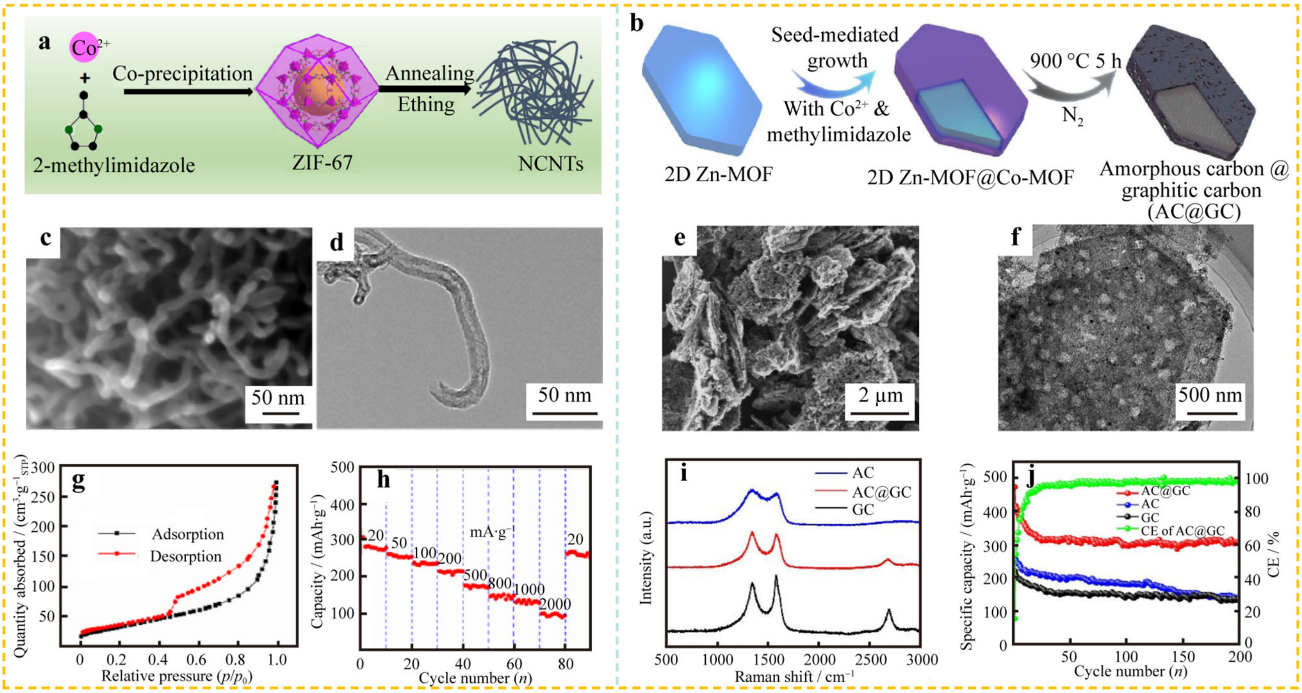

Fig. 3 **a** Schematic of preparation process of N-doped carbon nanotubes (NCNTs); **b** schematic synthesis of amorphous carbon/graphitic carbon nanoplates (AC@GC); **c** SEM image and **d** TEM image of NCNTs; **e** SEM image and **f** TEM image of AC@GC; **g** N_2 adsorption–desorption isotherms and **h** rate capacities under 20–2000 mA·g^{-1} of NCNTs; **i** Raman spectrum and **j** cycling performances of AC, AC@GC, GC. **a**, **c**, **d**, **g**, **h** Reproduced with permission from Ref. [39]. Copyright 2018, Wiley–VCH. **b**, **e**, **f**, **i**, **j** Reproduced with permission from Ref. [41]. Copyright 2019, the Royal Society of Chemistry

prepared carbon onions present high ionic diffusion kinetics, excellent mechanical stability, and a small layer size. When used in KIBs, HCONs delivered 105 mAh·g^{-1} at 10 A·g^{-1} and a long-term cycling performance of 132 mAh·g^{-1} at 2 A·g^{-1} after 5000 cycles. During the pyrolysis process of the MOF nanoparticles, they aggregated into bulks with irregular morphology, which could reduce reactive specific surface area and degrade the electrochemical performance of active materials. In this regard, Li et al. [42] synthesized a nitrogen-doped carbon with a honeycomb architecture through pyrolysis and subsequent acid-etching of MOFs/layered double hydroxides (LDHs) nanosheet hybrids. These features could effectively improve ionic conductivity and provide more active sites for potassium ion storage. Therefore, the prepared electrode can exhibit outstanding cycling capacity of 143 mAh·g^{-1} at 1 A·g^{-1} after 2000 cycles.

Compared with low-dimensional carbon materials, 3D carbon materials usually possess abundant micropores, mesopores, and excellent structural stability, which are beneficial for attaining enhanced cycling performance and rate capacity. Ingeniously, Zhang et al. [43] found that a nanosized ZIF-67 containing a Co center can result in spontaneous welding and generate 3D porous carbon networks. The fabricated process is shown in Fig. 4a; the pyrolysis of micrometer-sized MOF reveals large carbon particles, while the pyrolysis of reduced nanosized MOF shows carbon networks. Accordingly, SEM images (Fig. 4b) show carbon particles with polyhedral morphology that are produced from micrometer-sized ZIF-67, and every particle is separate. In contrast, continuous 3D carbon networks, rather than individual particles produced from nanosized ZIF-67, are shown in Fig. 4c. As indicated from the HRTEM results, both of the interlayer spacing of carbon samples were ~ 0.340 nm, which were larger than that of graphite (0.335 nm), demonstrating that Co nanoparticles can catalyze the graphitization. Importantly, the particle size of ZIF-67 can be decreased by adding trimethylamine. Moreover, graphite-connected carbon networks can be formed from a single Co nanoparticle catalyzing more MOF particles.

In addition to the skillful use of Co-catalyzed nanosized MOF particles to form 3D networks, the template method is also an effective strategy to prepare 3D carbon materials. In this way, Zhou et al. [44] fabricated an interconnected nitrogen-doped hierarchical porous carbon (N-HPC) by carbonizing 3D-ordered macroporous ZIF-8. The preparation process of N-HPC is shown in Fig. 4d. First, the ordered 3D polystyrene spheres (PS) monolithic filter cakes used as a sacrificial template were immersed in the ZIF-8 precursor solution. Next, the 3D-ordered macro-

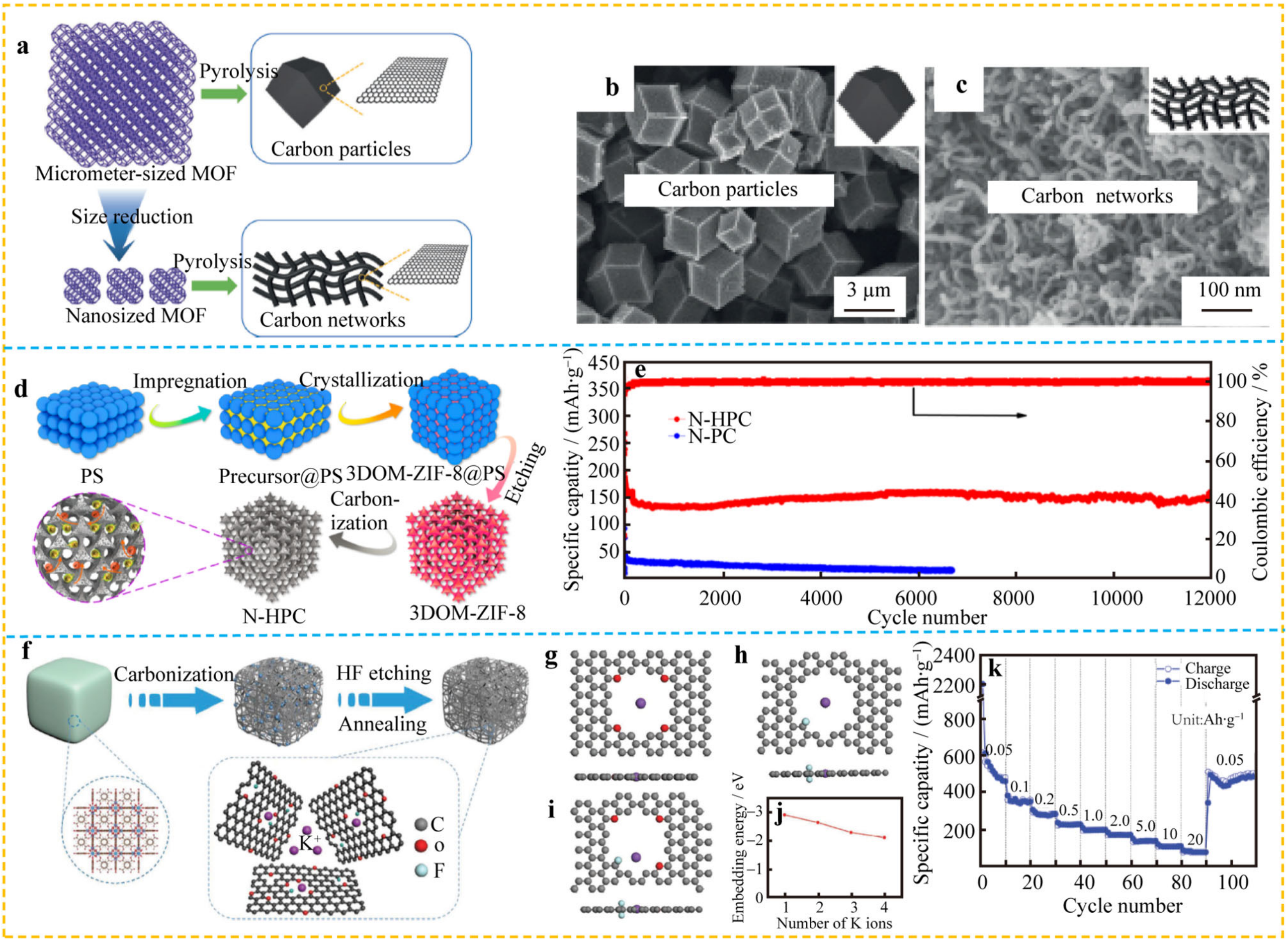

Fig. 4 **a** Formation mechanism of carbon particles and graphitic carbon networks; **b**, **c** SEM images of products. Reproduced with permission from Ref. [43]. Copyright 2017, Wiley–VCH. **d** Synthesis process of N-HPC and **e** cycle performance at 2 A·g^{-1}. Reproduced with permission from Ref. [44]. Copyright 2019, American Chemical Society. **f** Fabrication process of oxygen/fluorine dual-doped porous carbon nanopolyhedra (OFPCN); optimized model simulated by DFT calculations of one potassium atom insertion in **g** O, **h** F-doped porous carbon, and **i** OFPC, respectively; **j** K-embedding energy with increase of K atoms in OFPC; **k** rate capability of OFPCN. Reproduced with permission from Ref. [46]. Copyright 2019, WILEY–VCH

microporous ZIF-8 (3DOM-ZIF-8) was attained after removing the PSs template by etching. Finally, the N-HPC was synthesized via calcination at 900 °C in an Ar atmosphere. In the N-HPC structure, periodic macropores can improve the infiltration of the liquid electrolyte in the whole electrode, alleviating the concentration polarization; the interconnected micropores and ultrathin walls render improved mass transfer and electrolyte accessibility through the whole system. In addition, the G peak signal of in situ Raman spectra was very weak at the full potassiation state due to interference between the metallic-like behavior of intercalation compounds and the resonant phonon scattering process, indicating the adsorption storage mechanism of N-HPC. When applied in KIBs, N-HPC shows an excellent cycle stability of 157 mAh·g^{-1} after 12,000 cycles at 2.0 A·g^{-1} and nearly 100% coulombic efficiency (Fig. 4e).

In addition, heteroatom-doped carbon materials have abundant defects for K-ion adsorption. For example, pyridinic N with a lone pair of electrons could store potassium ions and enhance the specific capacity of the material. Because chemical bonds in MOF may disintegrate or react under different calcination temperatures, to control and enhance the pyridinic N content in carbon product, Li et al. [38] studied N-doped porous carbon with a high pyridine N content synthesized by optimizing the ZIF-67 pyrolysis temperature (600 °C was the optimized temperature, marked as NPC-600) as the anode material for KIBs. As a result, NPC-600 can deliver an excellent rate performance (186.2 mAh·g^{-1} at 2 A·g^{-1}) and cycling stability (231.6 mAh·g^{-1} at 0.5 A·g^{-1} after 2000 cycles). Moreover, S-doping is an effective strategy to improve the interlayer of carbonaceous materials, which is a promising strategy for relieving volume changes during the ion insertion/extraction process. Hence, Li and coworkers [45] further reported the nitrogen and sulfur co-doped carbon (NSC) microboxes with increased interlayer spacing derived from S-doped ZIF-67. The lower ratio of capacitance contribution of NSC investigated by the cyclic voltammetry (CV) data at different scan rates indicated that the insertion behavior of K-ions was dominant in the K-ion storage, which was verified by the reversible interlayer space in the ex situ TEM images during the potassiation/depotassiation process. As a result, the NSC displayed an interlayer spacing of 0.412 nm, and delivered a favorable cycle life (180.5 $mAh·g^{-1}$ at 0.5 $A·g^{-1}$ after 1000 cycles) and an excellent rate capacity (155.6 $mAh·g^{-1}$ at 2 $A·g^{-1}$).

In addition to N-doped carbon materials, due to F with high electronegativity, F-doped carbon could also result in adequate surface defects; moreover, oxygen-doped carbon materials can enhance the wettability and present more active sites. In this regard, Lu et al. [46] synthesized oxygen/fluorine dual-doped porous carbon nanopolyhedra (OFPCN) via HF etching and subsequent annealing process as a novel anode for KIBs. The prepared process is shown in Fig. 4f. Density functional theory (DFT) calculations investigate the K-adsorption ability of O or F dual-doped porous carbon, as shown in Fig. 4g–h. The O-doped and F-doped porous carbon can both maintain original structures after large K-atom insertion, and their adsorption energies (ΔE) are − 1.95 and − 2.12 eV, respectively. When embedding the K atom in the O/F dual-doped porous carbon, the carbon structure presents little distortion (Fig. 4i) and its ΔE is − 2.91 eV. Figure 4j shows that with the increase in embedded K atoms in OFPCN, ΔE gradually decreases but maintains negativity, manifesting a stable reaction and structure. In addition, CV measurements at various scan rates demonstrated the mixed mechanism during the charge storage process (the calculated b-value in the equation $i = av^b$ was 0.75, where i is the current response in CV, a and b are constants, and v is the scan rate). When used in KIBs, the OFPCN electrode in Fig. 4k shows an excellent reversible rate performance of 481, 360, 199, and 111 $mAh·g^{-1}$ at current densities of 0.05, 0.10, 1.00, 10.00 $A·g^{-1}$, respectively, and attains 512 $mAh·g^{-1}$ at a return current density of 0.05 $A·g^{-1}$. Regarding two-element doped carbon materials, nitrogen/oxygen co-doped mesoporous carbon octahedra (MCO) were also reported, which were synthesized using a carbonization-etching process of Cu-BTC (1,3,5-benzenetricarboxylic acid) [47]. The MCO electrode delivered excellent cycling performance of 100 $mAh·g^{-1}$ at 1 $A·g^{-1}$ after 1300 cycles.

Based on the above reports, through (1) designing appropriate MOF-derived carbon structures such as carbon nanotubes, carbon nanosheets, and 3D carbon networks, (2) combining those with the advantages of amorphous carbon and graphite carbon and (3) introducing heteroatoms into carbon materials, the rate capability and cycling performance of MOF-derived carbon materials in KIBs can be improved effectively. These strategies have the advantages of improving structural stability and electrolyte infiltration, guaranteeing small volume changes and a low redox plateau for high energy density, and increasing defects for more active sites and stronger K-ion adsorption ability. The ion storage mechanisms of MOF-derived carbon materials can be investigated using ex situ XRD, in situ Raman, ex situ Raman, ex situ HRTEM, and CV tests at different scan rates. In addition, their storage mechanisms are insertion or adsorption, which are mainly dependent on the degree of graphitization or defects, respectively.

2.2.2 *MOF-derived metal-based materials*

In a preparation process similar to that of MOF-derived carbon, MOF-derived metal-based materials are synthesized through annealing MOFs but reserving the metal centers. With subsequent phosphorization, sulfuration, or selenylation, metallic compounds coated in carbon frameworks can be fabricated. Compared with MOF-derived carbon, MOF-derived metal-based materials exhibit more multiple-reaction mechanisms, such as alloying and conversion reactions, providing controllable properties in KIBs.

Based on the phase diagram, Zn could react with K at room temperature [48]. Hence, Yan et al. [48] prepared Zn nanoparticles confined in a nanoporous carbon network (ZNP/C) and investigated its performance in KIBs for the first time. The synthetic procedure of ZNP/C is shown in Fig. 5a. The Zn-containing MOF (ZIF-8) is prepared by mixing zinc ions and dimethyl imidazole, then carbonizing the mixture at 600 °C to attain ZNP/C-600. During the annealing process, organic constituents form a porous carbon network; zinc metal centers are simultaneously transformed to zinc nanoparticles which are highly dispersed in the carbon matrix. Moreover, as the HRTEM image (Fig. 5b) and selected area electron diffraction (SAED) pattern (Fig. 5c) of ZNP/C-600 show, no distinct lattice fringes (no graphitized carbon) or no bright diffraction rings (no metallic Zn crystals) can be found, implying an amorphous structure. In the CV tests, the peak of KZn_x appeared/disappeared in 0.01/1.20 V at the scan rate of 0.2 $mV·s^{-1}$ over several cycles, implying the reversible alloying/dealloying of ZNP/C-600 for K-ion storage. The electrochemical test in Fig. 5i shows that ZNP/C-600 can retain 200 $mAh·g^{-1}$ at 100 $mA·g^{-1}$ after 100 cycles.

In addition, Bi and Sb metal are also alloying-type materials [49, 50]. To alleviate capacity loss of the Bi-based electrode during the potassiation/depotassiation

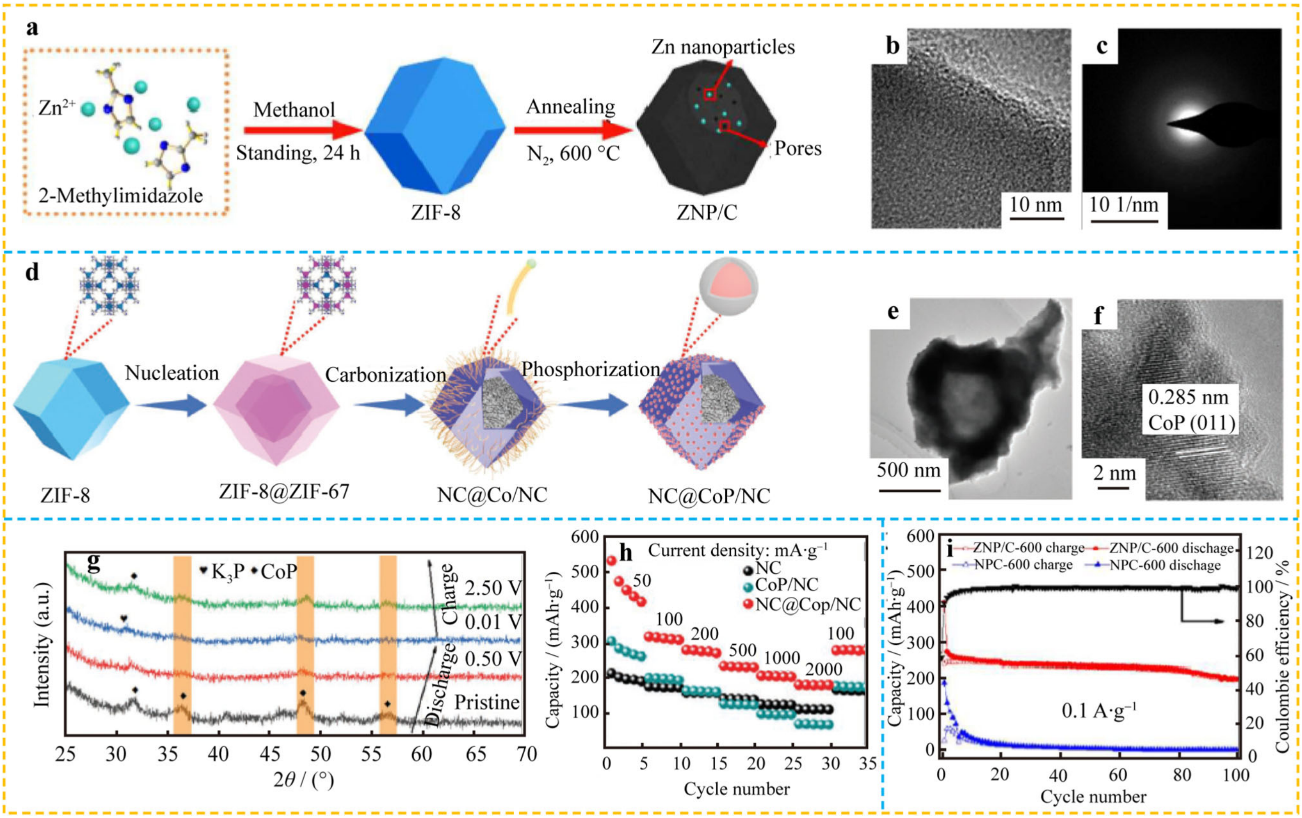

Fig. 5 **a** Formation mechanism of Zn nanoparticles confined in nanoporous carbon network (ZNP/C), **b** corresponding HRTEM image and **c** SAED pattern of ZNP/C-600; **d** schematics of fabricated N-doped carbon confined CoP polyhedron (NC@CoP/NC), **e** corresponding TEM image, **f** HRTEM image, **g** ex situ XRD spectra, and **h** rate performances of electrode; **i** cycling capacities of ZNP/C-600 and NPC-600. **a–c**, **i** Reproduced with permission from Ref. [48]. Copyright 2018, the Royal Society of Chemistry. **d–h** Reproduced with permission from Ref. [52]. Copyright 2020, WILEY–VCH

processes, Su et al. [49] prepared ultrathin carbon film@-carbon nanorods@Bi nanoparticles (UCF@CNs@BiN). In this unique structure, carbon nanorods can not only provide channels for ion diffusion, but can also accommodate the volume change of the Bi electrode during cycles. In the CV test at 0.01 $\mathrm{mV \cdot s^{-1}}$, three pairs of reduction/oxidation peaks, 0.75/0.64 V, 0.30/0.71 V, and 0.20/1.19 V, could be assigned to the alloying/dealloying of KBi_2/K_3Bi_2, K_3Bi_2/KBi_2, and K_3Bi/Bi, respectively. As a result, UCF@CNs@BiN materials exhibited an excellent steady capacity of ~ 327 $\mathrm{mAh \cdot g^{-1}}$ at 100 $\mathrm{mA \cdot g^{-1}}$ after 600 cycles with a low capacity decay of 0.038% per cycle.

CoP and FeP present recent high research interest due to their high specific capacity with the conversion reaction mechanism [51–54]. However, particle agglomeration and large volume change during the discharge process result in fast capacity decay. To solve these problems, Yi et al. [52] improved the design of NC@CoP/NC composites encompassing a CoP/N-doped carbon shell and an N-doped carbon core. The prepared process is shown in Fig. 5d. The Zn-containing MOF ZIF-8 is first prepared and used as template to grow ZIF-67.

By elevating the carbonization temperature to 700 °C, Zn particles evaporate and Co particles are retained. After further oxidization and subsequent phosphatization, the unique structure consists of a hollow carbon core, and a CoP modificatory carbon shell can be fabricated. TEM image (Fig. 5e) further demonstrates the hollow core–shell structure. In addition, HRTEM image (Fig. 5f) shows that CoP nanoparticles are embedded in carbon shell. The designed architecture can provide fast conductivity and favorable mechanical robustness and can prevent CoP nanoparticle agglomeration. For the reaction mechanism of CoP with K, ex situ XRD patterns (Fig. 5g) and ex situ HRTEM images substantiate the reversible conversion reaction due to the discharge product of K_3P/Co in 0.01 V and the charge product of CoP in 2.50 V. The rate property of NC@CoP/NC in KIBs (Fig. 5h) shows ~ 200 $\mathrm{mAh \cdot g^{-1}}$ at 2000 $\mathrm{mA \cdot g^{-1}}$, which benefits from electrode robustness and advantageous reaction mechanism. Similarly, FeP was confined in a porous carbon framework derived from MOF materials to solve the agglomeration issue and improve conductivity of electrode materials [52].

In sum, MOF-derived metal phosphides could exhibit favorable cycling and rate performances.

Likewise, confining metal chalcogenides in MOF-derived carbon can exhibit enhanced cycling stability and rate performance in KIBs. For example, Miao et al. [55] prepared a novel integrated 3D AC@CoS/NCNTs/CoS@CNFs network. The prepared process and structure illustration are shown in Fig. 6a. The carbon nanofibers (CNFs) fabricated via electrospinning are used as a template to grow MOFs. After carbonization, oxidation, and vulcanization, carbon-coated CoS nanoparticles form on the top of carbon nanotubes, and the end of the nanotubes are embedded in the CoS-coated carbon nanofibers. HRTEM images (Fig. 6b, c) demonstrate that CoS nanoparticles are encapsulated in amorphous carbon and grow on the top of carbon nanotubes. The unique 3D-ordered structure design can effectively reduce the ion diffusion path and enhance conductivity and mechanical stability, which are beneficial for excellent cycling performance. Through the CV test and ex situ XRD analysis, Co/K_2S and CoS can form reversibly in ~ 0.9 and 1.7 V during the potassiation/depotassiation process. As shown in Fig. 6g, the AC@CoS/NCNTs/CoS@CNFs electrode delivers more favorable cycling capacity than pristine CoS and NCNFs at 3.2 A·g^{-1}.

Recently, MOF-derived carbon materials used as templates to introduce other metal sulfides were investigated in KIBs [56–58]. This was accomplished after the

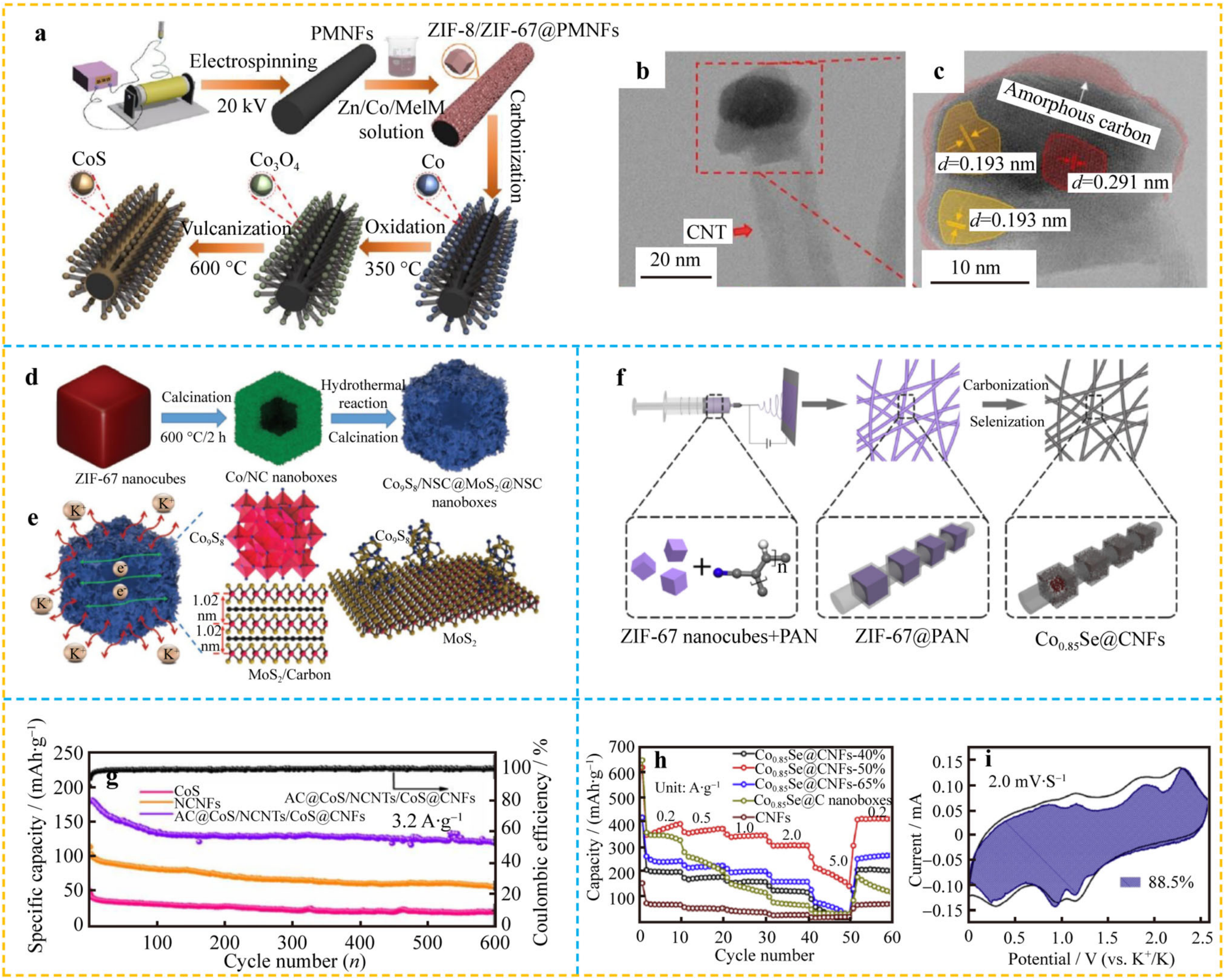

Fig. 6 **a** Schematic illustration of synthesis of AC@CoS/NCNTs/CoS@CNFs, and corresponding **b**, **c** HRTEM images; schematic illustration of **d** synthesis procedure and **e** transport process of K-ions and structural models of Co_9S_8/NSC@MoS_2@NSC nanoboxes; **f** formation mechanism of $Co_{0.85}Se$@CNFs; **g** cycling performances of AC@CoS/NCNTs/CoS@CNFs at 3.2 A·g^{-1}; **h** rate capacities of $Co_{0.85}Se$@CNFs with different weight ratios of ZIF-67/PAN precursor, $Co_{0.85}Se$@C nanoboxes, and CNFs; **i** cyclic voltammogram profile. **a**–**c**, **g** Reproduced with permission from Ref. [55]. Copyright 2019, the Royal Society of Chemistry. **d**, **e** Reproduced with permission from Ref. [57]. Copyright 2019, WILEY–VCH. **f**, **h**, **i** Reproduced with permission from Ref. [61]. Copyright 2019, Elsevier

carbonization of Co-containing MOFs, followed by the addition of Mo sources and thiourea to prepare Co_9S_8/NSC@MoS_2@NSC using a solvothermal process followed by calcination (Fig. 6d), where 0D Co_9S_8 nanoparticles grow on 2D MoS_2 nanosheets with an expanded interlayer space and a 3D N, S co-doped hollow carbon framework as the host (Fig. 6e) [57]. In this composite structure, the merits of Co_9S_8 with high electronic conductivity and MoS_2 with high ionic conductivity are reserved and enhanced. In the CV curves, the formation/oxidation of metallic Mo and Co occurred in 0.36/1.52 V and 1.20/1.85 V, respectively, implying the reversible K-ion storage of MoS_2 and Co_9S_8. In addition, the 3D hierarchical nanoboxes with excellent structure integrity greatly improves cycling stability and exhibits a high capacity of 141 $mAh \cdot g^{-1}$ at 3000 $mA \cdot g^{-1}$ in KIBs.

In addition, metallic selenides derived from typical MOFs ZIF-67 [59–61], ZIF-8 [62], Fe/Zn-MOF-5 [63] were synthesized and investigated in KIBs. Ingeniously, Etogo et al. [61] designed freestanding $Co_{0.85}Se$@carbon nanoboxes ($Co_{0.85}Se$@C) confined in carbon nanofibers films via electrospinning ZIF-67 and PAN, followed by a pyrolysis–selenidation process, as shown in Fig. 6f. In comparison with the aforementioned advantages of a porous carbon framework, the conductive carbon nanofiber network can not only improve the electronic conductivity but also stabilize the pristine structure during repeated K-ion insertion/deinsertion. Through optimizing the $Co_{0.85}Se$ content in $Co_{0.85}Se$@CNFs, the $Co_{0.85}Se$@CNFs with 51 wt% $Co_{0.85}Se$ exhibits suitable specific capacity and excellent conductivity. Ulteriorly, its CV test at 0.2 $mV \cdot s^{-1}$ and ex situ XRD at 0.2 $A \cdot g^{-1}$ in the range of 0.01–2.60 V demonstrated the formation of K_2Se_5/$Co_{0.85}Se$ in 0.54/2.6 V. However, K_2Se_5 decomposed into K and Se in 0.01 V and K_2Se_5 was partially converted to $Co_{0.85}Se$, which both adversely affected the high capacity for $Co_{0.85}Se$. When tested in KIBs, as shown in Fig. 5h, i, optimized $Co_{0.85}Se$@CNFs show 303 $mAh \cdot g^{-1}$ at high current density of 2 $A \cdot g^{-1}$ and high capacitive contribution of 88.5% at 2 $mV \cdot s^{-1}$.

In general, on account of MOF-derived porous carbon materials, the alloying reaction and the conversion reaction are both K^+-ion storage mechanisms for MOF-derived metal-based materials. Specifically, metal phosphides have a lower reduction potential than that of metal sulfides and metal selenides. Moreover, metal selenides are partially reversible during the potassiation/depotassiation process. Fortunately, metal nanoparticles, metal phosphides, metal sulfides, or metal selenides can be uniformly dispersed in carbon framework. These unique structures usually possess these advantages: (1) N doping derived from organic chains can provide more active sites for K-ion storage, (2) the high specific area is beneficial for electrolyte infiltration, (3) porous carbon frameworks provide enough space to accommodate volume change of metal-based materials during cycles in KIBs, (4) metal-based materials confined in carbon network can prevent nanoparticles aggregation, (5) carbon matrix and nanosized metal-based materials can improve electronic conductivity and reduce ion diffusion channels, respectively. As a result, improved electrochemical performance of electrode materials could be attained in KIBs.

2.3 Summary

MOFs exhibit excellent K-ion storage. For example, pristine MOFs have reactive active components and ion channels, which are beneficial for the insertion and extraction of ions. In addition, MOF-derived carbon materials usually present a porous structure and a large surface area. These characteristics are beneficial for providing sufficient space to accommodate the volume change during K-ion insertion/extraction, improving the infiltration of electrolyte and electrode materials, shortening ion diffusion paths, and further enhancing K-ion storage performance. Interestingly, heteroatoms from organic ligands in MOFs can dope into the carbon product during the carbonization process and generate abundant defects. Moreover, these defects can enhance electronic conductivity and reactivity by regulating electron distribution and producing additional active sites. As a result, the enhanced adsorption behavior (pseudocapacitance effect) can improve the rate performance and cycling stability. In addition, after the pyrolysis of MOFs, metal nanoparticles are uniformly dispersed in carbon frameworks. The alloying reaction of metal and K provides a high capacity. Meanwhile, the porous carbon can accommodate volume changes during alloying/dealloying. Furthermore, the subsequent phosphorization, sulfuration, or selenylation can create metal phosphide, metal sulfide, or metal selenide, respectively. These compounds enable high capacity in KIBs due to conversion and alloying reactions.

2.4 Prussian blue (PB)

PB and PB analogue (PBA) consist of transition metal ions coordinated with the organic chain of –CN–, and possess large channels for ion transport. Specifically, potassium-based PBAs have the chemical formula of $K_xM[Fe(CN)_6]_y \cdot mH_2O$ (M are transition metals, $0 \leq x \leq 2$, $y \leq 1$), where nitrogen-coordinated transition metal and carbon-coordinated Fe form open frameworks together bridged by cyanide groups $(–C{\equiv}N–)^-$. After introducing other nitrogen-coordinated transition metal ions (not Fe), the obtained PBA demonstrates performance in structure stability, redox centers, and discharge voltage plateaus different from those of pristine PB. In addition, the composites of PB or PBA with other conductive materials can demonstrate excellent conductivity and improved structural integrity. Furthermore, PB- or PBA-derived materials (e.g., metal phosphide, metal sulfide, or metallic selenide) used as anode materials in KIBs can present excellent conductivity and particle dispersibility due to their robust precursor structures and in situ formed carbon frameworks. Based on the above advantages, PB, PBA, and their composites and derivatives have potential for K-ion storage. Their electrochemical performances are shown in Table 2 [64–97].

2.5 Pristine PB

PB, with a facile synthesis process and stable structure, can reversibly store K^+ with a small Stokes radius [64, 65]. PB (the chemical formula is $K_aFe_b[Fe(CN)_6]_c{\cdot}nH_2O$) can be attained by adjusting the stoichiometric ratio. Different stoichiometric ratios in PB influence the charge state of the C–Fe^{III}/Fe^{II} couple and the N–Fe^{III}/Fe^{II} couple. In addition, PB in various electrolyte conditions can exhibit different K-ion diffusion kinetics. For example, Stilwell et al. [98] demonstrated that the low pH (pH = 2–3) of aqueous electrolyte was important for enhancing the cycle stability.

As PB has big channels for reversible K-ion insertion/extraction, PB was reported in KIBs and exhibited an excellent cycling capacity of ~ 70 mAh·g^{-1} after 500 cycles at 0.1 C (1 C = 87.36 mA·g^{-1}) [64]. Zampardi et al. [99] investigated the electrochemical behaviors of the PB toward K^+ (de-)insertion under different conditions and proved that the K^+ insertion into PB (which was converted to Prussian White, $K_2Fe^{II}[Fe^{II}(CN)_6]$) was dominant at the ensemble level, and that K^+ extraction from PB (which formed Berlin Green/Prussian Yellow, Fe^{III} $[Fe^{III}(CN)_6]$) was dominant at the single particle level. By adjusting PB particle sizes, $K_2Fe^{II}[Fe^{II}(CN)_6]$ can be mostly oxidated to Fe^{III} $[Fe^{III}(CN)_6]$ to achieve high specific capacity [66, 67]. In this regard, Su et al. [66] prepared potassium iron (II) hexacyanoferrate dehydrate ($K_2Fe^{II}[Fe^{II}(CN)_6]{\cdot}2H_2O$) nanocubes by changing the solvent from water to ethylene glycol with mild reducibility. As shown in Fig. 7a, the structural models of prepared $K_2Fe^{II}[Fe^{II}(CN)_6]{\cdot}2H_2O$ along different directions show two kinds of iron atoms which occupy the nitrogen-coordinated sites and the carbon-coordinated sites, forming $Fe^{II}N_6$ octahedra and $Fe^{II}C_6$ octahedra, respectively (Fig. 7c). The H_2O (1621 cm^{-1}) and divalent iron (~ 2060 cm^{-1}) in the $K_2Fe^{II}[Fe^{II}(CN)_6]{\cdot}2H_2O$ are confirmed by the FTIR spectrum (Fig. 7b).

And the $K_2Fe^{II}[Fe^{II}(CN)_6]{\cdot}2H_2O$ nanocubes are shown in Fig. 7d, the corresponding TEM image and fast Fourier transform (FFT) patterns in Fig. 7e show the *d*-spacing of 0.508 nm toward two vertical directions. When used in KIBs, except new peaks from K-ions insertion, the major diffraction peaks are reserved during cycles (Fig. 7h), implying the stability of the $K_2Fe^{II}[Fe^{II}(CN)_6]{\cdot}2H_2O$ crystal structure. And, these diffraction peaks of (011), (200), and (400) shifted monotonically toward higher diffraction angles when charging up to 1.2 V, where the *bc* plane occurred shrinkage accompanied by a slight expansion along the *a*-axis. The initial structure was restored when discharging to 0 V with a slightly expanded crystal structure. Furthermore, ex situ FTIR spectra (Fig. 7i) and a Gatan parallel EELS (Fig. 7j) of the $K_2Fe^{II}[Fe^{II}(CN)_6]{\cdot}2H_2O$ electrodes demonstrate the reversible valence state change of divalent ferricyanide (FTIR, 2060 cm^{-1}; EELS, ≈ 707.5 eV) and trivalent ferricyanide (FTIR, 2142 cm^{-1}; EELS, ≈ 708.0 and 711.3 eV) during the first charge/discharge processes. Owing to the $K_2Fe^{II}[Fe^{II}(CN)_6]{\cdot}2H_2O$ can provide two electrons per formula unit, the electrodes exhibit high reversible capacities of 107, 92, and 84 mAh·g^{-1} at current densities of 500, 2000, and 3000 mA·g^{-1} after 500 cycles in aqueous electrolyte, respectively (Fig. 7m). As demonstrated in Fig. 7n, the $K_2Fe^{II}[Fe^{II}(CN)_6]{\cdot}2H_2O$ battery delivers a specific energy of ≈ 65 Wh·kg^{-1} at the specific power of 1250 W·kg^{-1}, which shows potentially competitive against lead-acid and nickel metal-hydride batteries.

In nonaqueous electrolyte, PB materials are also widely investigated as electrodes in KIBs. For example, Zhang et al. reported $K_{0.220}Fe[Fe(CN)_6]_{0.805}{\cdot}\square_{0.195}{\cdot}4.01H_2O$ (where □ means vacancy) synthesized through mixing $K_4Fe(CN)_6$ and $FeCl_3$, and conducted an evaluation of electrochemical performance in the range of 2.0–4.0 V [68]. The products with uniform sizes of 20–30 nm are shown in Fig. 7f. The interplanar spacings of 0.50, 0.36, and 0.24 nm correspond to the diffraction planes of (200), (220), and (420), respectively (Fig. 7g). The nanoscale structure is beneficial for K^+ diffusion during cycles. When used as cathode materials in KIBs, the interstitial water in $K_{0.220}Fe[Fe(CN)_6]_{0.805}{\cdot}\square_{0.195}{\cdot}4.01H_2O$ led to low CE because of the decomposition of residual water with an increase in voltage. Moreover, the CE would increase with the amount of residual water decrease in subsequent cycles. The CV curves in Fig. 7k show unchanged anodic peaks and cathodic peaks after the initial cycle, which are attributed to the reversible redox reaction process of the C–Fe^{III}/Fe^{II} couple. The unchanged cubic structure based on ex situ XRD patterns during cycling can be attributed to this redox-active couple, where the amount of the intercalated cations is no more than an average of 1 cation per formula. Furthermore, the full cells of $K_{0.220}Fe[Fe(CN)_6]_{0.805}{\cdot}\square_{0.195}{\cdot}4.01H_2O$//commercial carbon materials exhibit 68.5 mAh·g^{-1} at 0.1 A·g^{-1} and maintain 93.4% capacity retention after 50 cycles.

Table 2 Electrochemical performances of Prussian blue (PB), PB analog (PBA), their composites and derivatives in KIBs

Samples	VW/VP/V	Cyclability/ CD/Cycles/ ($mAh\cdot g^{-1}/mA\cdot g^{-1}$)	RC/CD/ ($mAh\cdot g^{-1}/ mA\cdot g^{-1}$)	Electrolyte	Refs.
Pristine PB					
$KFe[Fe(CN)_6]$	$\sim$ 2.6–4.1	70/87.36/500	–	1 M KBF_4 in EC/DMC	[64]
Cubic PB crystals	0–1.1	78/500/900	80/500	0.5 M K_2SO_4 aqueous	[65]
$K_2Fe^{II}[Fe^{II}(CN)_6]\cdot 2H_2O$	0.01–1.2	107/500/500	109/1000	0.5 M K_2SO_4 aqueous	[66]
$K_{1.92}Fe[Fe(CN)_6]_{0.94}\cdot 0.5H_2O$	2.0–4.3/3.25	$\sim$ 110/65/100	$\sim$ 100/1300	0.8 M KPF_6 EC/DEC/FEC	[67]
$K_{0.220}Fe[Fe(CN)_6]_{0.805}\cdot\square_{0.195}\cdot 4.01H_2O$	2.0–4.0	52.4/200/100	36/400	0.8 M KPF_6 in EC/DEC	[68]
$K_{1.4}Fe_4[Fe(CN)_6]_3$	2.0–4.0	72/50/40	24.9/600	0.5 M KPF_6 in EC/DEC/FEC	[69]
$KFe[Fe(CN)_6]_{0.82}\cdot 2.87H_2O$	2.0–4.5	73/100/1000	40.6/500	1 M KPF_6 in EC/DEC/PC	[70]
5% Ni-doped PB	2.0–4.5	102.57/100/300	80.95/400	0.8 M KPF_6 in EC/DEC/FEC	[71]
PBA					
$K_{1.49}Ni_{0.36}Co_{0.64}[Fe(CN)_6]_{0.91}\cdot 0.89H_2O$	2.0–4.5/ $\sim$ 3.7	84/20/50	$\sim$ 42/200	0.8 M KPF_6 in EC:DM/FEC	[72]
$K_{0.6}Ni_{1.2}Fe(CN)_6\cdot 3.6H_2O$	0.4–1	$\sim$47/$\sim$ 500/5000	39/2500	1 M KNO_3 Electrolyte pH = 2	[73]
NiHCFe nanoparticles	$\sim$ 0.4–1	–	57.7/1C	1 M KNO_3 in H_2O	[74]
$K_2NiFe^{II}(CN)_6$	2.0–4.2/ $\sim$ 3.6	71.2/12/100	51.7/1800	0.5 M KPF_6 and 0.5 M $LiPF_6$ in EC/DMC	[75]
$Co_3[Co(CN)_6]_2\cdot 10.7H_2O$	0.05–2	297.5/100/200	221/1000	1.5 M KFSI in EC:DEC	[76]
$K_{1.75}Mn[Fe(CN)_6]_{0.93}\cdot 0.16H_2O$	2.0–4.5/3.8	$\sim$ 130/30/100	108/1000	0.7 M KPF_6 in EC:DEC	[77]
$K_{1.6}Mn[Fe(CN)_6]_{0.96}\cdot 0.27H_2O$	3.2–4.3/ > 3.8	75.5/50/30	60/200	1 M KFSI in PC:FEC	[78]
$K_{1.70}Mn[Fe(CN)_6]_{0.90}\cdot 1.10H_2O$	2.5–4.6/3.6	$\sim$ 100/156/100	–	Saturated $KClO_4$ in PC/FEC	[79]
$K_{0.3}Ti_{0.75}Fe_{0.25}[Fe(CN)_6]_{0.95}\cdot 2.8H_2O$	1.0–4.5/ > 1.6	73.1/100/100	58.9/500	0.8 M KPF_6 in EC:DMC/FEC	[80]
$K_2Zn_3[Fe(CN)_6]_2$	2.5–4.4/4	–	$\sim$62/0.1C	1 M KPF_6 in 1:1 DMC:EC	[81]
$K_{1.88}Zn_{2.88}[Fe(CN)_6]_2(H_2O)_{5.0}$	3.3–4.2/3.9	55.6/13.8/100	$\sim$ 38/138	0.5 M KPF_6 in EC:DEC/FEC	[82]
$K_{0.08}Zn_{1.44}[Fe(CN)_6]$	− 0.2–1.2	–	69.7/300	0.5 M K_2SO_4 aqueous solution	[83]
$K_{1.68}Fe_{1.09}Fe(CN)_6\cdot 2.1H_2O$	2.0–4.5/3.2	90.4/20/100	–	0.8 M KPF_6 in PC/FEC	[84]
$Fe^{III}Fe^{III}(CN)_6$	0–1	30.3/500/1100	–	saturated KCl aqueous solution	[85]
$K_{1.69}Fe[Fe(CN)_6]_{0.90}\cdot 0.4H_2O$	2–4.6/3.2	$\sim$ 70/100/300	–	0.5 M KPF_6 in EC/DEC/FEC	[86]
$K_{1.93}Fe[Fe(CN)_6]_{0.97}\cdot 1.82H_2O$	-0.4–1	88.2/1500/300	40/9000	1 M KNO_3 aqueous solution	[87]
$K_{1.9}Na_{0.1}Mn[Fe(CN)_6]\cdot 0.4H_2O$	2–4.5	106.4/75/100	$\sim$ 70/1500	0.8 M KPF_6 in EC/DEC/FEC	[88]
PB/PBA composites and derivatives					
NCoHCFe-K	− 0.3–1	150/670/2000	$\sim$155/1330	0.1 M KCl aqueous solution	[89]
MWCNT-PB	− 0.4–0.6	–	2.7 $mAh\cdot cm^{-3}$/ 0.02	0.1 M KCl aqueous solution	[90]
RGO@PB@SSM	2–4/3.3	52.1/100/305	35/1000	0.8 M KPF_6 in EC/DEC/FEC	[91]
$K_{1.85}Mn[Fe(CN)_6]_{0.98}\&_{0.02}\cdot 0.7H_2O$	2–4.5/4	103.2/750/500	100.2/1500	0.8 M KPF_6 in EC/DEC/FEC	[92]
PB/MoS_2	− 0.5–1.3	121/10,000/10,000	215/1000	0.5 M K_2SO_4 aqueous solution	[93]
$K_{1.87}Fe[Fe(CN)_6]_{0.97}\cdot\square_{0.03}\cdot 0.84 H_2O$@PPy	2–4.2	61.8/1000/500	60/1000	0.8 M KPF_6 in EC/DEC	[94]
Ni–Fe–S–CNT	0–3	181/100/50	54/800	0.8 M KPF_6 in EC/DEC	[95]
Ni–Fe–P/NC	0.01–3.0	287/100/500	75.6/1000	1 M LiTFSI in DOL/DME/$LiNO_3$	[96]
Mn–Fe–Se/CNTs	0–3	141/50/70	83/800	0.8 M KPF_6 in DEC/EC	[97]

PB: Prussian blue, VW: voltage window, VP: voltage platform, CD: current density, RC: rate capability, MWCNT: multiwalled carbon nanotube, RGO: reduced graphene oxide, SSM: stainless-steel meshes, NC: N-doped carbon, PPy: polypyrrole, EC: ethylene carbonate, DMC: dimethyl carbonate, DEC: diethyl carbonate, FEC: fluoroethylene carbonate, PC: propylene carbonate, M: $mol\cdot L^{-1}$

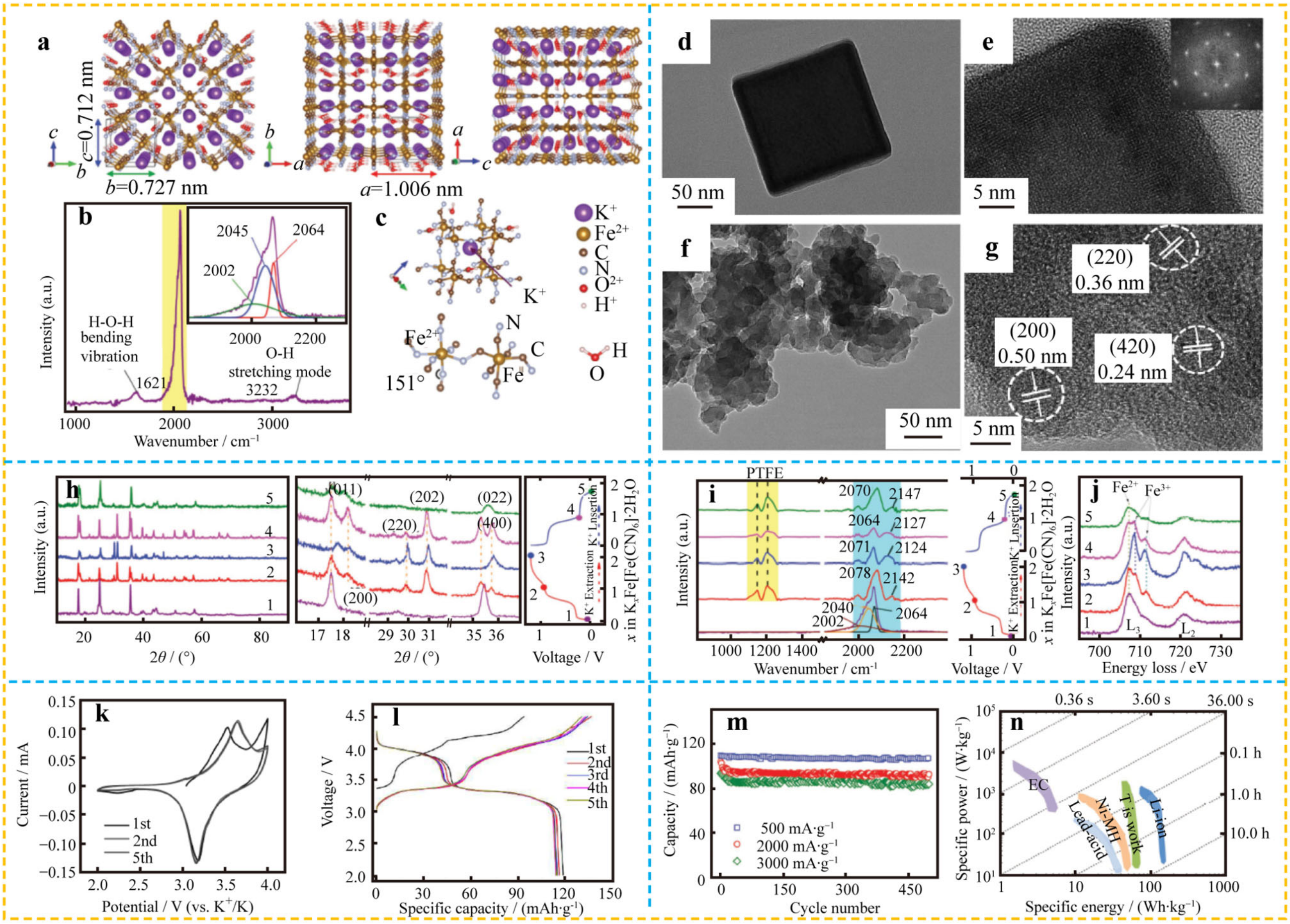

Fig. 7 **a** Refined crystal structure of potassium iron hexacyanoferrate dihydrate, **b** corresponding Fourier transform infrared spectroscopy (FTIR) spectrum (inset presenting enlarged image), **c** unit formula, **d** TEM image and **e** HRTEM image, inset in **e** presenting FFT patterns; **f** TEM image, **g** HRTEM image of potassium Prussian blue nanoparticles (KPBNPs); **h** ex situ XRD patterns of $K_2Fe^{II}[Fe^{II}(CN)_6]\cdot 2H_2O$ at the first cycle, **i** corresponding ex situ FTIR spectra, and **j** electron energy loss spectroscopy (EELS) spectra of iron cation; **k** CV curves of KPBNPs/K half-cell at 0.1 $mV\cdot s^{-1}$; **l** charge/discharge curves of $KFe^{II}[Fe^{III}(CN)_6]$ (KFFCN) at 10 $mA\cdot g^{-1}$; **m** cycling performance of $K_2Fe^{II}[Fe^{II}(CN)_6]\cdot 2H_2O$ at 0.5, 2.0, and 3.0 $A\cdot g^{-1}$, and **n** corresponding specific energy versus power in aqueous KIBs. **a–e**, **h–j**, **m**, **n** Reproduced with permission from Ref. [66]. Copyright 2016, WILEY–VCH. **f**, **g**, **k** Reproduced with permission from Ref. [68]. Copyright 2016, WILEY–VCH. **l** Reproduced with permission from Ref. [70]. Copyright 2017, the Royal Society of Chemistry

Recently, Qin and coworkers [69] synthesized $K_{1.4}Fe_4[Fe(CN)_6]_3$ ultrathin nanosheets via the precursor of $K_3Fe(CN)_6$ and optimizing the aging time. They found that PB particles could be entirely converted into PB nanosheets by increasing the aging time to 48 h. The reassembled hierarchical structure of the nanosheets exhibited superior K-ion storage in nonaqueous electrolyte, and delivered 72 $mAh\cdot g^{-1}$ at 0.05 $A\cdot g^{-1}$ after 40 cycles in the range of 2.0–4.0 V based on one redox-active site of the $N–Fe^{III}/Fe^{II}$ couple, where the reactive site was confirmed by ex situ Raman since CN^- is very sensitive to the coordinating Fe. To further enhance the cycling performance of the electrode, Chong et al. [70] prepared $KFe[Fe(CN)_6]_{0.82}\cdot 2.87H_2O$ nanoparticles (KFFCN) of 15–20 nm through a simple hydrothermal process using $K_3Fe(CN)_6$ and $FeCl_2\cdot 4H_2O$. In the testing voltage window of 2.0–4.5 V, there are two pairs of plateaus, which indicate the two redox-active sites of C and N-coordinated Fe^{II}/Fe^{III} redox couples (Fig. 7l). During the first discharge process, the discharging plateau was elongated by a large margin, which indicated that the material was activated from $KFe^{II}[Fe^{III}(CN)_6]$ to $K_2Fe^{II}[Fe^{II}(CN)_6]$ after the initial charge–discharge process (Fig. 7l). Benefiting from the two redox-active sites of C- and N-coordinated Fe^{II}/Fe^{III} redox couples, the KFFCN electrode exhibited an excellent capacity of 73 $mAh\cdot g^{-1}$ at 0.1 $A\cdot g^{-1}$ after 1000 cycles and maintained an 80.49% capacity retention. When reducing particles to nanoscale, a small quantity of nickel doping can also improve the electrochemical properties and motivate the C-coordinated $Fe^{2+/3+}$ redox couple of PB. As reported by Huang et al. [71], $K_2Ni_{0.05}Fe_{0.95}[Fe(CN)_6]$ can enhance the current density of the $Fe^{2+}N_6/Fe^{3+}N_6$ redox couple at a low potential and of the $Fe^{2+}C_6/Fe^{3+}C_6$ redox couple at a high potential. As a result, the $K_2Ni_{0.05}Fe_{0.95}[Fe(CN)_6]$ delivered the discharge capacity from ~ 40 to 53 mAh·g^{-1} at a high-voltage plateau, and exhibited 102.57 mAh·g^{-1} at 100 mA·g^{-1} after 300 cycles in the range of 2–4.5 V.

In PB, the electrochemical performance is dependent upon the two redox centers of N-coordinated Fe^{2+}/Fe^{3+} (in low potential) and C-coordinated Fe^{2+}/Fe^{3+} (in high potential). Among them, the N-coordinated Fe^{2+}/Fe^{3+} redox reaction is dominated by large particles. Reducing particle size, introducing defects, or element doping can activate the redox reaction of C-coordinated Fe^{2+}/Fe^{3+}. In addition, the Fe value of precursors, synthetic strategy, and testing voltage window all could be important for C-coordinated Fe^{2+}/Fe^{3+}. Specifically, Fe^{2+} in the product and a large testing voltage window (2.0–4.5 V) are beneficial for adding redox centers. Furthermore, tuning the synthetic strategy to reduce the $[Fe(CN)_6]^{4-}$ vacancies and crystal water in PB is beneficial for reversible K-ion storage. The above strategies demonstrate enhanced electrochemical performance for PB in KIBs.

2.6 PB analog (PBA)

Similar to the preparation process of PB, PBA materials are synthesized through introducing other metals to replace N-coordinated Fe. PBA possesses a 3D open framework and its general chemical formula is $A_xM_aFe_b(CN)_6\cdot nH_2O$ (A are alkali cations; M are transition metals, such as Ni, Co, Mn, Ti, Zn). Among them, Fe is coordinated at the carbon end of the –C≡N– group at low spin states, and M atoms are coordinated at the nitrogen end of the –C≡N– group at high spin states. The transition metal ions linked to nitrogen can affect the redox performance of PBA [72]. Hence, different transition metal ions are introduced into PB to attain PBA with an adjustable electrochemical performance.

Ni-PBA can exhibit a long cycling life in KIBs. For example, Wessells et al. [73] reported a prolonged reversible insertion/extraction of potassium ions in a nickel hexacyanoferrate (NiHCF) electrode material in aqueous electrolytes. The nanoparticulate (20–50 nm) NiHCF with improved crystallinity was synthesized at 70 °C. In the crystal structure, transition metal cations Fe and Ni are coordinated with carbon and nitrogen, respectively, forming a face-centered cubic structure, as shown in Fig. 8a. The K-ions can insert into the framework and occupy the interstitial "A" sites. Ex situ XRD patterns of the K-ion insertion process reveal that the lattice parameter increased where the isotropic lattice strain was 1.1% during potassium cycling, which corresponded to an increase in the radius of $[Fe^{2+}(CN)_6]^{4-}$ during their oxidation to $[Fe^{3+}(CN)_6]^{3-}$. Owing to this low strain, NiHCF exhibited no capacity loss during the first 1000 cycles and a capacity loss of 1.75%/1000 cycles in subsequent cycles. Later, Lee et al. [74] demonstrated that nickel hexacyanoferrate (NiHCFe) could exhibit a variety of different electrochemical behaviors in aqueous and organic electrolytes. Based on the CV results, NiHCFe in an aqueous electrolyte with symmetric anodic/cathodic peaks (at similar potential vs. SHE(V)) show superior electrochemical kinetics to NiHCFe in propylene carbonate with asymmetric anodic/cathodic peaks (at different potential vs. SHE(V)). However, due to the low redox of H_2O, the PBA could not attain a high energy density [30].

To improve ion diffusion and energy density, Zheng et al. [75] constructed an asymmetric battery. In this battery, the cathode was $K_2NiFe^{II}(CN)_6$, the anode was commercial graphite, and the organic electrolyte consisted of 0.5 mol·L^{-1} $LiPF_6$ and 0.5 mol·L^{-1} KPF_6 in EC/DMC (1:1, volume ratio). In accordance with the redox peaks in the CV tests, the schematic of the reaction process is shown in Fig. 8g. K-ions and Li-ions reversibly intercalate the cathode side and anode side, respectively. The design combined advantages of $K_2NiFe^{II}(CN)_6$ and graphite. As a result, the asymmetric battery exhibits a high working voltage (~ 3.6 V) and an excellent cycling performance with no capacity fading during 5000 cycles (Fig. 8h). It is worth noting that Ni-PBA shows one redox peak couple, which is attributed to the redox of C-coordinate Fe. The inactive Ni can construct robust ion diffusion channels for enhanced cycling performance.

To further improve specific capacity, a potential strategy is to introduce active transition metals into PB, such as Mn, Co, or Ti. For example, Huang et al. [72] reported $K_2Ni_xCo_{1-x}Fe(CN)_6$ with various Co/Ni ratios. The Ni and Co are connected to the N end. The conventional $K_2CoFe(CN)_6$ cathode barely maintained its structure during fast charging/discharging, which was attributed to the two redox reactions of $Co^{2+/3+}$ and $Fe^{2+/3+}$ at both ends of the cyanide bridges. As mentioned above, the doping of inactive Ni may balance the structural disturbances during K^+ insertion/extraction. The product $K_{1.49}Ni_{0.36}Co_{0.64}Fe(CN)_6\cdot 0.89H_2O$ ($PBN_{0.4}C_{0.6}$) exhibited better-optimized conductivity and capacity than did PBC($K_{1.61}Co[Fe(CN)_6]_{0.89}\cdot 0.76H_2O$) and PBN($K_{1.55}Ni[Fe(CN)_6]_{0.93}\cdot 2.01H_2O$). In CV testing, as compared with the PBC with two redox peaks at 4.08/3.65 V (redox reaction of $Fe^{2+/3+}$) and 3.31/3.00 V (redox reaction $Co^{2+/3+}$), $PBN_{0.4}C_{0.6}$ and PBN had distinct redox peaks at ~ 4.23/3.58 V, and the peak areas of $PBN_{0.4}C_{0.6}$ were larger than those of PBN due to the partial redox reaction of $Co^{2+/3+}$. In KIBs, $PBN_{0.4}C_{0.6}$ delivered a capacity of 84.28 mAh·g^{-1} after 50 cycles, which is much higher than that of PBN and PBC. Interestingly, Deng et al. [76] reported $Co_3[Co(CN)_6]_2$ synthesized using $K_3[Co(CN)_6]$

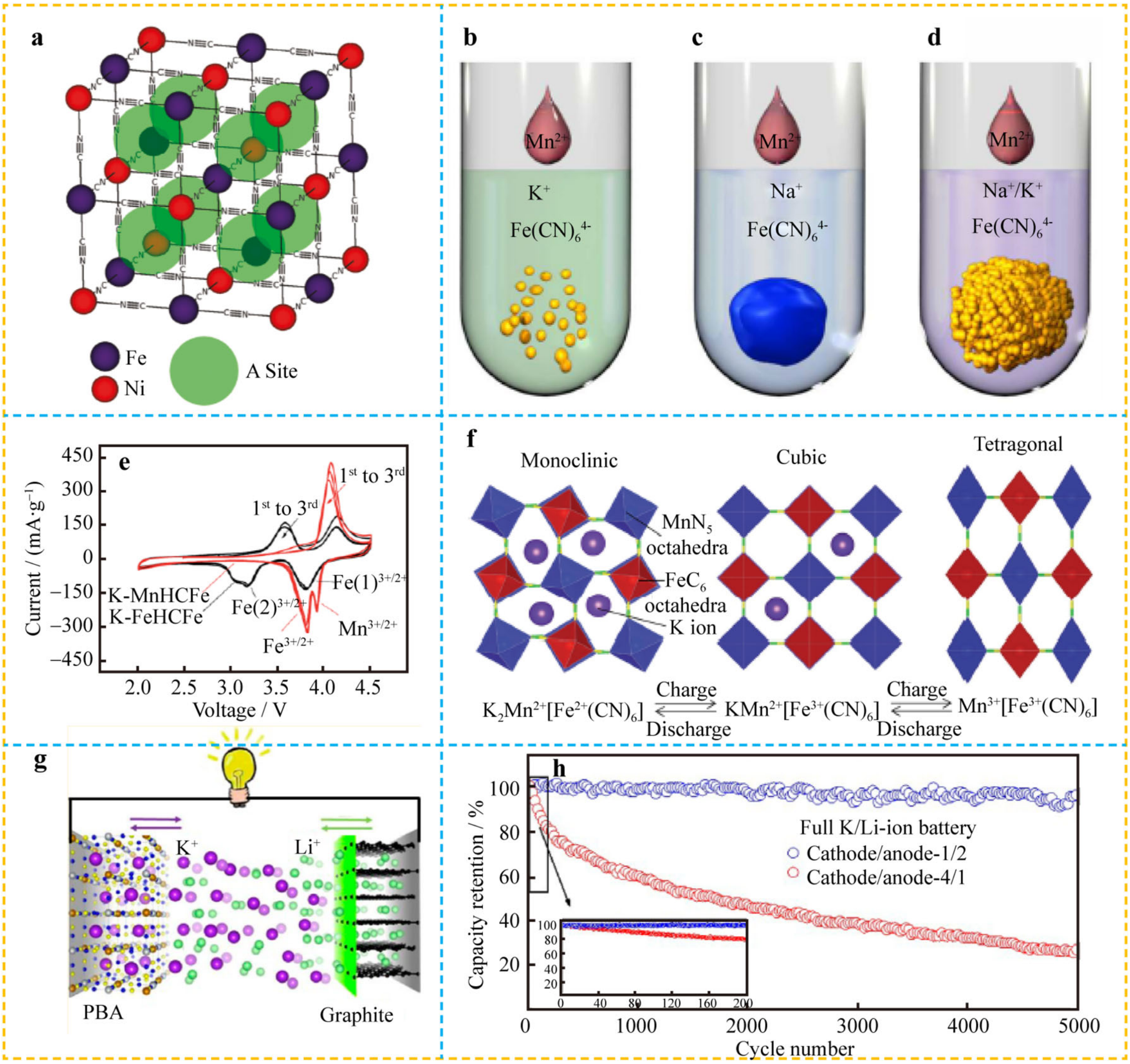

Fig. 8 **a** Crystal structure of NiHCF. Reproduced with permission from Ref. [73]. Copyright 2011, American Chemical Society. Schematic synthetic process of **b** $K_xMnFe(CN)_6$ in K^+ precursors, **c** $Na_yMnFe(CN)_6$ in Na^+ precursors, **d** $K_xMnFe(CN)_6$ in Na^+ and K^+ mixed precursors. Reproduced with permission from Ref. [79]. Copyright 2017, American Chemical Society. **e** Cyclic voltammograms of K-FeHCFe and K-MnHCFe, and **f** phase transition and crystal structures of K-MnHCFe during charge/discharging. Reproduced with permission from Ref. [77]. Copyright 2017, the Royal Society of Chemistry. **g** Working mechanism of asymmetric K/Li-ion battery and **h** cycling (based on cathode) retention at 1.8 A·g^{-1} in full batteries. Reproduced with permission from Ref. [75]. Copyright 2017, American Chemical Society

and $Co(CH_3COO)_2·4H_2O$ as raw materials. In the $Co_3[Co(CN)_6]_2$ structure, the Co^{2+} connects octahedral $[Co(CN)_6]^{3-}$ complexes to form a face-centered cubic structure. When used as anode materials in KIBs, Co^{2+} and $[Co(CN)_6]^{3-}$ can be reduced to Co and $[Co(CN)_6]^{5-}$, respectively. As a result, the as-prepared $Co_3[Co(CN)_6]_2$ delivered a reversible capacity of 324.5 mAh·g^{-1} at 0.05–2.00 V (vs. K^+/K).

Similarly, Bie et al. [77] introduced active Mn into PB and synthesized $K_{1.75}Mn[Fe^{II}(CN)_6]_{0.93}·0.16H_2O$ (K-MnHCFe) using a convenient precipitation method. The CV curve of K-MnHCFe (Fig. 8e) shows two reduction peaks (3.81 and 3.92 V), which correspond to the redox reaction of $Fe^{2+/3+}$ and $Mn^{2+/3+}$, respectively. In addition, through operando XRD measurement, the electrode shows a reversible structural change from monoclinic to tetragonal (Fig. 8f). Owing to the two redox active centers and excellent mechanical stability, the electrode delivered a high capacity of 137 mAh·g^{-1} in K half-cells. Even when used in a K-ion battery (graphite as anode electrode), the battery exhibited the discharge capacity of 60 mAh·g^{-1} (calculated on K-MnHCFe) at 2 A·g^{-1}. Regarding the compatibility between electrolyte and electrode materials, Jiang et al. [78] reported Mn-based PBA with an enhanced electrochemical performance in an optimized electrolyte. By changing the common potassium bis(fluorosulfonyl)imide (KFSI) ethylene carbonate:diethyl carbonate (EC:DEC) electrolyte to the KFSI ethylene carbonate:fluoroethylene carbonate (PC:FEC) electrolyte, a K-conducting passivation layer could be formed. As a result, the electrode delivered 115 mAh·g^{-1} in a KIB. Recently, Xue et al. [79] successfully prepared secondary particles using a precursor consisting of Na^+ and K^+ coexisting with a molar ratio of 1:1. The preparation illustration is shown in Fig. 8b–d. The fast crystallization rates in K^+ solution (small particles, ~ 40 nm) and slow crystallization rates in Na^+ solution (large particles, ~ 140 nm) result in secondary particles ($K_{1.70}Mn[Fe(CN)_6]_{0.90}\cdot 1.10H_2O$ (NI-KMHCF), of ~ 350 nm). The larger NI-KMHCF particles with a smaller external surface area can prevent more side reactions, especially at a high voltage. When used in KIBs, NI-KMHCF with larger particles and a smaller surface area can present improved cycling performance over that of KMHCF synthesized in a K^+ solution. Therefore, based on the two redox centers of Fe (at lower potential) and of Mn (at higher potential), Mn-based PBA could deliver a high theoretical capacity of 156 mAh·g^{-1}.

The Ti-based PBA with two pairs of redox peaks was also studied. For example, Luo et al. [80] reported potassium titanium hexacyanoferrate ($K_{0.3}Ti_{0.75}Fe_{0.25}[Fe(CN)_6]_{0.95}\cdot 2.8H_2O$, KTH) obtained by a simple co-precipitation of $TiCl_3$ and $KCl/K_4Fe(CN)_6$. The KTH shows the redox of Ti^{3+}/Ti^{4+} at 1.6/2.1 V and the material exhibited 136.7 mAh·g^{-1} at 50 mA·g^{-1} in the initial discharge. On the other hand, Zn-based PBA could usually present a higher discharge voltage (not lower than 3.9 V) than that of K/K^+ in a non-aqueous electrolyte [81, 82]. Although Zn-based PBA shows two pairs of redox peaks, only the C-coordinated Fe is electrochemically active [81–83]. The detailed intercalation mechanism is not understood clearly for the two redox couples with only one redox center. As a result, the Zn-based PBA has a low theoretical specific capacity of 69.08 mAh·g^{-1} based on $K_{1.88}Zn_{2.88}[Fe\ (CN)_6]_2(H_2O)_{5.0}$ [82].

In addition, other ferrocyanide and ferricyanide materials were also reported [84–88]. For example, Wu et al. [84] prepared Prussian white analogues, $K_xMFe(CN)_6\cdot mH_2O$ (M present Fe, Co, Ni, or Cu), using a simple precipitation method. They present different electrochemical performances due to varying water content, crystal defects, and crystal integrity. Among them, FeFe-Prussian white exhibits the highest capacity of 90.4 mAh·g^{-1} at 20 mA·g^{-1} after 100 cycles. Furthermore, smaller particle sizes can usually exhibit higher capacity performance. For instance, potassium ferricyanide (Prussian Green) with particle sizes of 50–70 nm can exhibit a higher capacity of 121.4 mAh·g^{-1} than PB with particles sizes of 2–10 μm (53.8 mAh·g^{-1}) [85]. Furthermore, He and Nazar [86] reported a different crystallite size and morphology of $K_{1.69}Fe[Fe(CN)_6]_{0.90}\cdot 0.4H_2O$ using a novel citrate chelation route. As a result, the optimal cathode material composed of the smallest crystallites (20 nm) delivered a reversible capacity of 120 mAh·g^{-1} at 100 mA·g^{-1}. In another study, Li et al. [87] studied potassium Prussian white analogues with different crystallinities and sizes prepared by regulating the acidity of the reactive solution. Finally, the prepared $K_{1.93}Fe[Fe(CN)_6]_{0.97}\cdot 1.82H_2O$ nanoparticles with high crystallinity presented a reversible capacity of 40 mAh·g^{-1} at a high current density of 9000 mA·g^{-1}.

Compared to PB, PBA materials exhibit improved electrochemical performances through introducing other metals into PB. For example, inactive Ni-based PBA exhibits ultralong cycling stability without a huge capacity loss. Active Co-based PBA, Mn-based PBA, and Ti-based PBA can provide two redox centers for K-ion insertion, and they exhibit high capacity. Although the aqueous electrolyte is cheap and beneficial for K-ion diffusion, it presents a low voltage window. The non-aqueous electrolyte has a high voltage window for high energy density. In addition, Mn-based PBA and Zn-based PBA both exhibit a high discharge voltage. Furthermore, optimizing electrolyte components and particle sizes are effective strategies for improving electrochemical performance.

2.7 PB/PBA composite and derivatives

PB or PBA materials have also been combined with other materials to form composites to improve performance for stability, structural integrity, and conductivity of materials.

PB or PBA composite can improve the effective conductivity and stability of pristine PB or PBA [89–92]. For example, Nossol et al. [90] reported flexible CNTs/PB nanocomposites through the liquid–liquid interfacial route, showing high reversible capacities of 2.7 mAh·cm^{-3} and a 74% capacity retention after 1000 cycles for MWCNT/PB. In addition, Zhu and coworkers [91] used rusty stainless-steel meshes (RSSM) as precursor to a synthesized binder-free reduced graphene oxide (RGO)@PB@SSM composite with an enhanced electrochemical performance. The preparation is illustrated in Fig. 9a. First, cleaned SSM is converted into RSSM in an aqueous ammonia solution. Then, the RSSM is soaked in the potassium ferrocyanide/hydrochloric acid solution. Fe and Ni ions from the metal oxide/hydroxide in the acid environment can react with ferricyanide ions to form PB@SSM. Finally, RGO@PB@SSM can be obtained through graphene oxide (GO) dip-coating and subsequent reduction in a potassium borohydride solution. The generated PB was dispersed in the interlayer between the RGO and the SMM, which could show robust physical contact with the RGO and SSM substrates. This could enable ultrafast electron transport and avoid the agglomeration of PB nanocubes. When used in KIBs, the RGO@PB@SSM electrode shows reversible redox peaks and a small potential gap of anodic and cathodic peaks in Fig. 9j. Owing to the improved stability and conductivity, the binder-free RGO@PB@SSM cathode delivers 35 $mAh \cdot g^{-1}$ at 1000 $mA \cdot g^{-1}$, as shown in Fig. 9k. Recently, Sun et al. [92] studied potassium manganese Prussian blue/graphene (KPB/G) nanocomposite, prepared using a ball-milling method, as an electrode in KIBs. The KPB particles with small sizes resulting from ball-milling were uniformly loaded onto graphene. The KPB/G electrode exhibited an improved electrochemical performance of 100.2 $mAh \cdot g^{-1}$ at 10 C, which was an improvement over the 39.6 $mAh \cdot g^{-1}$ at 10 C for pristine KPB (1 C = 150 $mA \cdot g^{-1}$).

PB or PBA-based composites with materials other than carbon are also reported [93, 94, 100]. For example, PB/MoS_2-based nanocomposites were synthesized using an MoS_2 flake as a conductive matrix for the homogeneous nucleation of PB nanocrystals [93]. The mechanically exfoliated MoS_2 flake and PB/MoS_2 are characterized in Fig. 9b–f. The compact, ~ 40-nm-thick PB film is uniformly coated on MoS_2. Chemically exfoliated MoS_2 with a negative surface charge and selective functionalization benefits the homogeneous growth of the single-layer limited PB film with high porosity and small crystal size. Finally, the PB/MoS_2 obtained a high capacity retention of ≈ 97% after 10 000 cycles at 10 $A \cdot g^{-1}$. Xue et al. [94] proposed a polypyrrole/Prussian blue composite (KHCF@PPy) fabricated using an in situ polymerization coating method. The prepared KHCF@PPy shows improved structural integrity (low coordinated water content and reduced $[Fe(CN)_6]^{4-}$ vacancies) and conductivity over that of pristine KHCF. The optimized electrode delivered 61.8 $mAh \cdot g^{-1}$ after 500 cycles at 1000 $mA \cdot g^{-1}$, with an 85.7% capacity retention. Therefore, the PB- or PBA-based composites could exhibit enhanced electrochemical performances due to their improved structural integrity and conductivity.

Derivatives from PB or PBA and their composites are studied as anodes in KIBs [95–97]. For instance, the double-shelled Ni–Fe–P/N-doped carbon nanoboxes (defined as Ni–Fe–P/NC) were synthesized by Chen and coworkers, as illustrated in Fig. 9g [96]. First, FeFe@NiFe PBA was prepared using epitaxial deposition. Then, the FeFe@NiFe PBA was phosphatized at a low temperature to attain Ni–Fe–P/NC nanocubes. The dice-like Ni–Fe–P/NC shows an average diameter of ~ 350 nm, and its outer shells consist of numerous nanoparticles as shown in Fig. 9h. The gap between the inner and the outer shells is ~ 80 nm, as shown in Fig. 9i. As for the product, nitrogen-doped carbon could improve the conductivity. The robust structure could not only accommodate strain stress and prevent particle aggregation during charging/discharging, but could also provide an increase in surface area for enhancing reactivity. In CV testing of 0.01–3.00 V, after the first scan, the cathodic peaks steadily appeared at 0.55 V, corresponding to K^+ insertion, and the anodic peaks located at 1.98 V could be observed, corresponding to K^+ extraction. Based on the above advantages, the Ni–Fe–P/NC electrode delivered 287 $mAh \cdot g^{-1}$ at 0.1 $A \cdot g^{-1}$ after 500 cycles. Furthermore, Wang et al. [97] designed porous MnSe/$FeSe_2$ (Mn–Fe–Se)/CNT composites (Mn–Fe–Se/CNTs) synthesized through simple carbonization-selenization of Mn–Fe PBA/CNT. The prepared electrode delivered 141 $mAh \cdot g^{-1}$ after 70 cycles at 50 $mA \cdot g^{-1}$. The PB- or PBA-derived materials, such as sulfide, phosphide, and selenide can inherit the robust and porous structure of PB or PBA, and in situ formed N-doped carbon can improve the conductivity of the electrode. As a result, PB- or PBA-derived materials present enhanced capacity properties.

PB or PBA composites or derived materials exhibit improved electrochemical performance. PB or PBA composites present a low concentration of both vacancies and crystal water due to the induced growth from the high surface area and active sites. PB or PBA composites also show excellent conductivity because of their conductive additives. Hence, the composite electrodes deliver improved cycling and rate capacity. In addition, PB or PBA, comprised of metal centers and organic ligands, can be used as templates to prepare porous or hollow metal phosphides, metal sulfides, and metal selenides with robust structures and excellent conductivity. As a result, PB- or PBA-derived materials deliver improved K-ion storage performance as the anode in KIBs as compared to the storage performance for the corresponding pristine metal phosphides, metal sulfides, and metal selenides.

2.8 Summary

In PB materials, the electrochemical performances depend upon two redox centers of N-coordinated Fe^{2+}/Fe^{3+} (in low redox potential) and C-coordinated Fe^{2+}/Fe^{3+} (in high redox potential). Thorough ex situ Raman or CV testing can identify the redox centers due to CN^- being very sensitive to the coordinating Fe and the different redox potentials. The N-coordinated Fe^{2+}/Fe^{3+} redox reaction is dominated by huge particles. By reducing particle size, introducing element doping can improve the redox reaction of C-coordinated Fe^{2+}/Fe^{3+} in a high potential environment. Furthermore, tuning the synthetic strategy to reduce $[Fe(CN)_6]^{4-}$ vacancies and crystal water in PB benefits reversible K-ion storage. In addition, PBA materials exhibit improved electrochemical performance through the introduction of other metals into PB. For example, inactive Ni-based PBA exhibits ultralong cycling stability without a

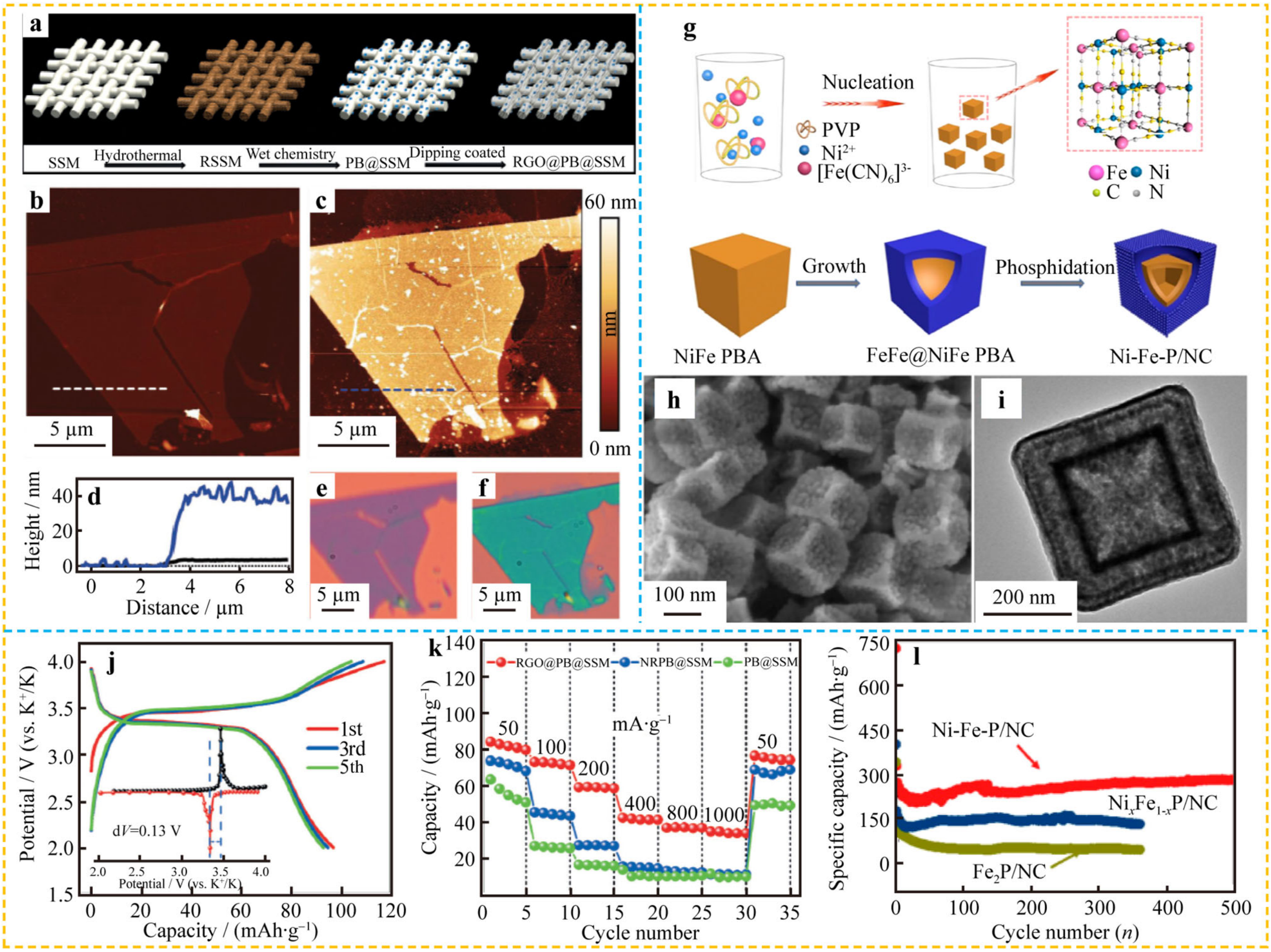

Fig. 9 **a** Schematic of preparation process of RGO@PB@SSM electrodes; atomic force microscope (AFM) images of exfoliated MoS_2 **b** before and **c** after mechanical treatment, **d** corresponding height profiles, and optical images **e** before and **f** after PB functionalization; **g** schematics of fabricated Ni–Fe–P/NC, and corresponding **h** SEM image and **i** TEM image; **j** discharge/charge curves of RGO@PB@SSM at 10 $mA \cdot g^{-1}$, inset being differential curve of the third cycle; **k** rate tests of NRPB@SSM, PB@SSM and RGO@PB@SSM; **l** cycling tests at 0.1 $A \cdot g^{-1}$ of Ni–Fe–P/NC, $Ni_xFe_{1-x}P$/NC and Fe_2P/NC electrodes. **a**, **j**, **k** Reproduced with permission from Ref. [91]. Copyright 2019, American Chemical Society. **b–f** Reproduced with permission from Ref. [93]. Copy 2017, WILEY–VCH. **g–i**, **l** Reproduced with permission from Ref. [96]. Copyright 2019, American Chemical Society

huge capacity loss. Active Co-based PBA, Mn-based PBA, and Ti-based PBA can provide two redox centers for K-ion insertion, and those materials exhibit high capacity. Furthermore, optimizing electrolyte components and particle sizes are effective strategies for improving the electrochemical performance of PBA. PB or PBA composites present low concentrations of vacancies and crystal water due to the induced growth from the higher surface area and the active sites. In addition, PB or PBA materials with metal centers and organic ligands can used as templates to prepare porous or hollow metal phosphides, metal sulfides, and metal selenides with robust structures and excellent conductivity. As a result, PB- or PBA-derived materials deliver enhanced K-ion storage performance as anodes in KIBs.

3 Conclusion and outlook

As mentioned above, metal coordination materials (including MOFs, PB, and PBA, along with their composites and derivatives) have been widely investigated in KIBs. Meanwhile, the metal coordination materials with large ion diffusion channels and robust structures can effectively improve K-ion diffusion kinetics and accommodate volume change during cycles for enhanced electrochemical performances. Particularly, composites or derivatives of PB, PBA, or MOFs can facilitate the reaction kinetics and present enhanced cycling capacity due to their excellent conductivity, rigid frameworks, and abundant active sites. In addition, through optimizing preparation technology such as reaction time and temperature, the condition of the solution, and calcination atmosphere, metal coordination materials with few structure defects, short ion diffusion distances, and abundant active sites can be attained. This review briefly summarizes the development of metal coordination materials as electrode materials in KIBs. With the increasing reports on metal coordination materials by various research groups, the electrochemical performances of these materials are gradually improved and their composites are continuously enriched. However, there are still challenges for the development of metal coordination materials in their performance and practical applications. Here, we list several challenges and available strategies for the development of metal coordination materials in KIBs.

1. Conductivities of metal coordination materials are poor. There are two strategies to ameliorate the conductivity. One strategy is to construct and exploit conductive metal coordination materials, based on their own characteristics. The other strategy is to introduce conductive materials (e.g., CNT, rGO, AC, conducting polymer, and ultrathin nanosheets) to enhance the conductivity of metal coordination materials.
2. Optimizing a prepared strategy for PB and PBA with fewer vacancies (such as $[Fe(CN)_6]^{4-}$ vacancies) and reduced crystal water through polymer coating and ultrathin nanosheets induces growth, which is beneficial for improving the structural stability of the electrode. Moreover, although the content of crystal water can be easily measured, the influence of a varied quantity of crystal water during K-ion storage is rarely investigated. In addition, the species and content of metal ions coordinated with N should be enriched and regulated, respectively, to deliver a high discharge capacity and a long cycling performance.
3. Regarding the metal coordination-based composites, including MOF-, PB-, and PBA-based composites and their derivatives, it is important to combine the advantages of all components and overcome the shortcomings of an individual component. Hence, during designing the composite, the high surface areas and abundant active sites of MOF, PB, PBA, and their derivatives should be maintained. Furthermore, the connection of all components in composites should be robust, which is crucial for displaying the synergistic effect.
4. Regarding their derivatives, the structure of metal coordination materials would be destroyed during carbonization, phosphorization, sulfuration, or selenylation. To maintain the morphology of the metal coordination material precursor, PB materials can be prepared by enhancing crystallinity using a higher reaction temperature [73], and MOF materials can be fabricated by introducing guest materials, such as MoS_2 [93] or polypyrrole [94].
5. Different kinds of metal coordination materials can be successfully prepared, such as MOF@PBA [100]. A series of issues on architectural design and electrochemical performance for their composites in KIBs could be investigated.
6. The electrochemical capacities of the presently known materials are still low for practical applications. This issue could be further resolved through constructing and exploiting metal coordination materials with sufficient reactive sites.

Finally, metal coordination materials can exhibit excellent cycling performance due to their large ion diffusion channels. However, tremendous efforts need to be devoted to exploiting metal coordination materials with better electrochemical performance.

Acknowledgements This work was financially supported by the Program for Changjiang Scholars and Innovative Research Team in University (No. IRT_16R21), the Chinese 02 Special Fund (No. 2017ZX02408003), the Scientific and Technological Project of Henan Province (No. 182102210297), the Open Fund of National Joint Engineering Research Center (Nos. HKDNM201807 and HKDNM2019017), the Science Foundation for Youths of Henan University of Science and Technology (No. 2013QN006), the Student Research Training Plan of Henan University of Science and Technology (No. 2020026) and the National Undergraduate Innovation and Entrepreneurship Training Program (No. 202010464031).

References

[1] Sui D, Xu LQ, Zhang HT, Sun ZH, Kan B, Ma YF, Chen YS. A 3D cross-linked graphene-based honeycomb carbon composite with excellent confinement effect of organic cathode material for lithium-ion batteries. Carbon. 2020;157:656.

[2] Ma XD, Xiong XH, Zou PJ, Liu WZ, Wang F, Liang LW, Liu Y, Yuan CZ, Lin Z. General and scalable fabrication of core–shell metal sulfides@C anchored on 3D N-doped foam toward flexible sodium ion batteries. Small. 2019;15(45):1903259.

[3] Li YX, Zhai XL, Liu Y, Wei HJ, Ma JQ, Chen M, Liu XM, Zhang WH, Wang GX, Ren FZ, Wei SZ. WO_3-based materials as electrocatalysts for hydrogen evolution reaction. Front Mater. 2020;7(105):105.

[4] Li JY, Zhang WM, Zhang X, Huo LY, Liang JY, Wu LS, Liu Y, Gao JF, Pang H, Xue HG. Copolymer derived micro/meso-porous carbon nanofibers with vacancy-type defects for high-performance supercapacitors. J Mater Chem A. 2020;8(5):2463.

[5] Shi ZJ, Feng WJ, Wang X, Li MM, Song CK, Chen LJ. Catalytic cobalt phosphide Co_2P/carbon nanotube nanocomposite as host material for high performance lithium–sulfur battery cathode. J Alloys Compd. 2020. https://doi.org/10.1016/j.jallcom.2020.156289.

[6] Zou PJ, Lin ZH, Fan MN, Wang F, Liu Y, Xiong XH. Facile and efficient fabrication of Li_3PO_4-coated Ni-rich cathode for high-performance lithium-ion battery. Appl Surf Sci. 2020;504:144506.

[7] Hao X, Zhao Q, Su S, Zhang S, Ma J, Shen L, Yu Q, Zhao L, Liu Y, Kang F, He YB. Constructing multifunctional

interphase between $Li_{1.4}Al_{0.4}Ti_{1.6}(PO_4)_3$ and Li metal by magnetron sputtering for highly stable solid-state lithium metal batteries. Adv Energy Mater. 2019;9(34):1901604.

[8] Wang X, Yang C, Xiong X, Chen G, Huang M, Wang JH, Liu Y, Liu M, Huang K. A robust sulfur host with dual lithium polysulfide immobilization mechanism for long cycle life and high capacity Li–S batteries. Energy Storage Mater. 2019;16:344.

[9] Zhao Q, Hao X, Su S, Ma J, Hu Y, Liu Y, Kang F, He YB. Expanded-graphite embedded in lithium metal as dendrite-free anode of lithium metal batteries. J Mater Chem A. 2019;7(26):15871.

[10] Li Y, Xu Y, Liu Y, Pang H. Exposing 001 crystal plane on hexagonal Ni-MOF with surface-grown cross-linked mesh-structures for electrochemical energy storage. Small. 2019;15(36):1902463.

[11] Yuan M, Guo X, Liu Y, Pang H. Si-based materials derived from biomass: synthesis and applications in electrochemical energy storage. J Mater Chem A. 2019;7(39):22123.

[12] Wang G, Chen C, Chen YH, Kang XW, Yang CH, Wang F, Liu Y, Xiong XH. Self-stabilized and strongly adhesive supramolecular polymer protective layer enables ultrahigh-rate and large-capacity lithium–metal anode. Angew Chem Int Ed Engl. 2020;59(5):2055.

[13] Li MM, Feng WJ, Wang X. The dual-play of carbon nanotube embedded with CoNi N codoped porous polyhedra toward superior lithium–sulfur batteries. J Alloys Compd. 2020;853:157194. https://doi.org/10.1016/j.jallcom.2020.157194.

[14] Wang F, Liu Y, Zhao YF, Wang Y, Wang ZJ, Zhang WH, Ren FZ. Facile synthesis of two-dimensional porous $MgCo_2O_4$ nanosheets as anode for lithium-ion batteries. Appl Sci-Basel. 2018;8(1):22.

[15] Liu Y, Wang HC, Yang KK, Yang YN, Ma JQ, Pan KM, Wang GX, Ren FZ, Pang H. Enhanced electrochemical performance of Sb_2O_3 as an anode for lithium-ion batteries by a stable cross-linked binder. Appl Sci-Basel. 2019;9(13):2677.

[16] Guo XT, Zhang YZ, Zhang F, Li Q, Anjum DH, Liang HF, Liu Y, Liu CS, Alshareef HN, Pang H. A novel strategy for the synthesis of highly stable ternary SiO_x composites for Li-ion-battery anodes. J Mater Chem A. 2019;7(26):15969.

[17] Liu G, Cui J, Luo R, Liu Y, Huang X, Wu N, Jin X, Chen H, Tang S, Kim J-K, Liu X. 2D MoS_2 grown on biomass-based hollow carbon fibers for energy storage. Appl Surf Sci. 2019;469:854.

[18] Liu Y, Wang Y, Wang F, Lei ZX, Zhang WH, Pan KM, Liu J, Chen M, Wang GX, Ren FZ, Wei SZ. Facile synthesis of antimony tungstate nanosheets as anodes for lithium-ion batteries. Nanomaterials. 2019;9(12):1689.

[19] Wang F, Liu Y, Wei HJ, Wang GX, Ren FZ, Liu XM, Chen M, Volinsky AA, Wei SZ, He Y-B. Graphene induced growth of Sb_2WO_6 nanosheets for high-performance pseudocapacitive lithium-ion storage. J Alloys Compd. 2020;839:9.

[20] Wang R, Cao X, Zhao D, Zhu L, Xie L, Liu J, Liu Y. Wet-chemistry synthesis of $Li_4Ti_5O_{12}$ as anode materials rendering high-rate Li-ion storage. Int J Energy Res. 2020;44(6):4211.

[21] Wang BP, Lv R, Lan DS. Preparation and electrochemical properties of Sn/C composites. Rare Met. 2019;38(10):996.

[22] Wu ZH, Yang JY, Yu B, Shi BM, Zhao CR, Yu ZL. Self-healing alginate-carboxymethyl chitosan porous scaffold as an effective binder for silicon anodes in lithium-ion batteries. Rare Met. 2019;38(9):832.

[23] Eftekhari A, Jian ZL, Ji XL. Potassium secondary batteries. ACS Appl Mater Int. 2017;9(5):4404.

[24] Sun Yi, Shi PC, Chen JJ, Wu QJ, Liang X, Rui XH, Xiang HF, Yu Y. Development and challenge of advanced nonaqueous sodium ion batteries. Energy Chem. 2020;2(2):100031.

[25] Chen Y, Zhuo SM, Li ZY, Wang CL. Redox polymers for rechargeable metal-ion batteries. Energy Chem. 2020;2(2):100030.

[26] Yu M, Yin Z, Yan G, Wang Z, Guo H, Li G, Liu Y, Li L, Wang J. Synergy of interlayer expansion and capacitive contribution promoting sodium ion storage in S, N-doped mesoporous carbon nanofiber. J Power Sources. 2020;449:227514.

[27] Luo W, Wan JY, Ozdemir B, Bao WZ, Chen YN, Dai JQ, Lin H, Xu Y, Gu F, Barone V, Hu LB. Potassium ion batteries with graphitic materials. Nano Lett. 2015;15(11):7671.

[28] Jian ZL, Xing ZY, Bommier C, Li ZF, Ji XL. Hard carbon microspheres: potassium-ion anode versus sodium-ion anode. Adv Energy Mater. 2016;6(3):1501874.

[29] Du M, Li Q, Zhao Y, Liu CS, Pang H. A review of electrochemical energy storage behaviors based on pristine metal–organic frameworks and their composites. Coord Chem Rev. 2020;416:213341.

[30] Zhou AJ, Cheng WJ, Wang W, Zhao Q, Xie J, Zhang WX, Gao HC, Xue LG, Li JZ. Hexacyanoferrate-type prussian blue analogs: principles and advances toward high-performance sodium and potassium ion batteries. Adv Energy Mater. 2020;35:2000943.

[31] Zheng SS, Xue HG, Pang H. Supercapacitors based on metal coordination materials. Coord Chem Rev. 2018;373:2.

[32] Li C, Hu X, Hu B. Cobalt(II) dicarboxylate-based metal-organic framework for long-cycling and high-rate potassium-ion battery anode. Electrochim Acta. 2017;253:439.

[33] An Y, Fei H, Zhang Z, Ci L, Xiong S, Feng J. A titanium-based metal–organic framework as an ultralong cycle-life anode for PIBs. Chem Commun. 2017;53(59):8360.

[34] Li C, Wang KB, Li JZ, Zhang QC. Nanostructured potassium-organic framework as an effective anode for potassium-ion batteries with a long cycle life. Nanoscale. 2020;12(14):7870.

[35] Liao J, Hu Q, Mu J, He X, Wang S, Chen C. A vanadium-based metal-organic phosphate framework material $K_2(VO)_2(HPO_4)_2(C_2O_4)$ as a cathode for potassium-ion batteries. Chem Commun. 2019;55(5):659.

[36] Deng QJ, Feng SS, Hui P, Chen HT, Tian CC, Yang R, Xu YH. Exploration of low-cost microporous Fe(III)-based organic framework as anode material for potassium-ion batteries. J Alloys Compd. 2020;830:154714.

[37] Liu S, Yang B, Zhou J, Song H. Nitrogen-rich carbon-onion-constructed nanosheets: an ultrafast and ultrastable dual anode material for sodium and potassium storage. J Mater Chem A. 2019;7(31):18499.

[38] Li Y, Yang C, Zheng F, Ou X, Pan Q, Liu Y, Wang G. High pyridine N-doped porous carbon derived from metal–organic frameworks for boosting potassium-ion storage. J Mater Chem A. 2018;6(37):17959.

[39] Xiong P, Zhao X, Xu Y. Nitrogen-doped carbon nanotubes derived from metal–organic frameworks for potassium-ion battery anodes. Chemsuschem. 2018;11(1):202.

[40] Lu G, Wang H, Zheng Y, Zhang H, Yang Y, Shi J, Huang M, Liu W. Metal–organic framework derived N-doped CNT@ porous carbon for high-performance sodium- and potassium-ion storage. Electrochim Acta. 2019;319:541.

[41] Li D, Cheng X, Xu R, Wu Y, Zhou X, Ma C, Yu Y. Manipulation of 2D carbon nanoplates with a core–shell structure for high-performance potassium-ion batteries. J Mater Chem A. 2019;7(34):19929.

[42] Li J, Li Y, Ma X, Zhang K, Hu J, Yang C, Liu M. A honeycomb-like nitrogen-doped carbon as high-performance anode for potassium-ion batteries. Chem Eng J. 2020;384:123328.

[43] Zhang W, Jiang X, Wang X, Kaneti YV, Chen Y, Liu J, Jiang JS, Yamauchi Y, Hu M. Spontaneous weaving of graphitic

carbon networks synthesized by pyrolysis of ZIF-67 crystals. Angew Chem Int Ed Engl. 2017;56(29):8435.

[44] Zhou X, Chen L, Zhang W, Wang J, Liu Z, Zeng S, Xu R, Wu Y, Ye S, Feng Y, Cheng X, Peng Z, Li X, Yu Y. Three-dimensional ordered macroporous metal–organic framework single crystal-derived nitrogen-doped hierarchical porous carbon for high-performance potassium-ion batteries. Nano Lett. 2019;19(8):4965.

[45] Li Y, Zhong W, Yang C, Zheng F, Pan Q, Liu Y, Wang G, Xiong X, Liu M. N/S codoped carbon microboxes with expanded interlayer distance toward excellent potassium storage. Chem Eng J. 2019;358:1147.

[46] Lu J, Wang C, Yu H, Gong S, Xia G, Jiang P, Xu P, Yang K, Chen Q. Oxygen/fluorine dual-doped porous carbon nanopolyhedra enabled ultrafast and highly stable potassium storage. Adv Funct Mater. 2019;29(49):1906126.

[47] Xia GL, Wang CL, Jiang P, Lu J, Diao JF, Chen QW. Nitrogen/oxygen co-doped mesoporous carbon octahedrons for high-performance potassium-ion batteries. J Mater Chem A. 2019;7(19):12317.

[48] Yan C, Gu X, Zhang L, Wang Y, Yan L, Liu D, Li L, Dai P, Zhao X. Highly dispersed Zn nanoparticles confined in a nanoporous carbon network: promising anode materials for sodium and potassium ion batteries. J Mater Chem A. 2018; 6(36):17371.

[49] Su S, Liu Q, Wang J, Fan L, Ma R, Chen S, Han X, Lu B. Control of SEI formation for stable potassium-ion battery anodes by Bi-MOF-derived nanocomposites. ACS Appl Mater Int. 2019;11(25):22474.

[50] Cheng N, Zhao JG, Fan L, Liu ZM, Chen SH, Ding HB, Yu XZ, Liu ZG, Lu BG. Sb-MOFs derived Sb nanoparticles@-porous carbon for high performance potassium-ion batteries anode. Chem Commun. 2019;55(83):12511.

[51] Miao W, Zhao X, Wang R, Liu Y, Li L, Zhang Z, Zhang W. Carbon shell encapsulated cobalt phosphide nanoparticles embedded in carbon nanotubes supported on carbon nanofibers: a promising anode for potassium ion battery. J Colloid Interface Sci. 2019;556:432.

[52] Yi Y, Zhao W, Zeng Z, Wei C, Lu C, Shao Y, Guo W, Dou S, Sun J. ZIF-8@ZIF-67-derived nitrogen-doped porous carbon confined CoP polyhedron targeting superior potassium-ion storage. Small. 2020. https://doi.org/10.1002/smll.201906566.

[53] Xu X, Feng J, Liu J, Lv F, Hu R, Fang F, Yang L, Ouyang L, Zhu M. Robust spindle-structured FeP@C for high-performance alkali-ion batteries anode. Electrochim Acta. 2019;312:224.

[54] Zhang ZF, Wu CX, Chen ZH, Li HY, Cao HJ, Luo XJ, Fang ZB, Zhu YY. Spatially confined synthesis of a flexible and hierarchically porous three-dimensional graphene/FeP hollow nanosphere composite anode for highly efficient and ultrastable potassium ion storage. J Mater Chem A. 2020;8(6):3369.

[55] Miao W, Zhang Y, Li H, Zhang Z, Li L, Yu Z, Zhang W. ZIF-8/ZIF-67-derived 3D amorphous carbon-encapsulated CoS/NCNTs supported on CoS-coated carbon nanofibers as an advanced potassium-ion battery anode. J Mater Chem A. 2019; 7(10):5504.

[56] Rui B, Li J, Chang L, Wang H, Lin L, Guo Y, Nie P. Engineering MoS_2 nanosheets anchored on metal organic frameworks derived carbon polyhedra for superior lithium and potassium storage. Front Energy Res. 2019;7:142.

[57] Yang C, Feng J, Zhang Y, Yang Q, Li P, Arlt T, Lai F, Wang J, Yin C, Wang W, Qian G, Cui L, Yang W, Chen Y, Manke I. Multidimensional integrated chalcogenides nanoarchitecture achieves highly stable and ultrafast potassium-ion storage. Small. 2019;15(44):1903720.

[58] Han Y, Li W, Zhou K, Wu X, Wu H, Wu X, Shi Q, Diao G, Chen M. Bimetallic sulfide Co_9S_8/N-C@MoS_2 dodecahedral heterogeneous nanocages for boosted Li/K storage. Chemnanomat. 2020;6(1):132.

[59] Xie J, Zhu Y, Zhuang N, Lei H, Zhu W, Fu Y, Javed MS, Li J, Mai W. Rational design of metal organic framework-derived FeS_2 hollow nanocages@reduced graphene oxide for K-ion storage. Nanoscale. 2018;10(36):17092.

[60] Ma G, Li C, Liu F, Majeed MK, Feng Z, Cui Y, Yang J, Qian Y. Metal-organic framework-derived $Co_{0.85}Se$ nanoparticles in N-doped carbon as a high-rate and long-lifespan anode material for potassium ion batteries. Mater. Today Energy 2018;10:241.

[61] Etogo CA, Huang H, Hong H, Liu G, Zhang L. Metal–organic-frameworks-engaged formation of $Co_{0.85}Se$@C nanoboxes embedded in carbon nanofibers film for enhanced potassium-ion storage. Energy Storage Mater. 2020;24:167.

[62] Hu Y, Lu T, Zhang Y, Sun Y, Liu J, Wei D, Ju Z, Zhuang Q. Highly dispersed ZnSe nanoparticles embedded in N-doped porous carbon matrix as an anode for potassium ion batteries. Part Part Syst Char. 2019;36(10):1900199.

[63] Yuan JJ, Liu W, Zhang XK, Zhang YH, Yang WT, Lai WD, Li XK, Zhang JJ, Li XF. MOF derived ZnSe–$FeSe_2$/RGO nanocomposites with enhanced sodium/potassium storage. J Power Sources. 2020;455:227937.

[64] Eftekhari A. Potassium secondary cell based on Prussian blue cathode. J Power Sources. 2004;126(1–2):221.

[65] Zhou L, Zhang M, Wang Y, Zhu Y, Fu L, Liu X, Wu Y, Huang W. Cubic Prussian blue crystals from a facile one-step synthesis as positive electrode material for superior potassium-ion capacitors. Electrochim Acta. 2017;232:106.

[66] Su D, McDonagh A, Qiao SZ, Wang G. High-capacity aqueous potassium-ion batteries for large-scale energy storage. Adv Mater. 2017;29(1):1604007.

[67] Liao J, Hu Q, Yu Y, Wang H, Tang Z, Wen Z, Chen C. A potassium-rich iron hexacyanoferrate/dipotassium terephthalate@carbon nanotube composite used for K-ion full-cells with an optimized electrolyte. J Mater Chem A. 2017;5(36):19017.

[68] Zhang C, Xu Y, Zhou M, Liang L, Dong H, Wu M, Yang Y, Lei Y. Potassium Prussian blue nanoparticles: a low-cost cathode material for potassium-ion batteries. Adv Funct Mater. 2017;27(4):1604307.

[69] Qin M, Ren W, Meng J, Wang X, Yao X, Ke Y, Li Q, Ma L. Realizing superior prussian blue positive electrode for potassium storage via ultrathin nanosheet assembly. ACS Sustain Chem Eng. 2019;7(13):11564.

[70] Chong S, Chen Y, Zheng Y, Tan Q, Shu C, Liu Y, Guo Z. Potassium ferrous ferricyanide nanoparticles as a high capacity and ultralong life cathode material for nonaqueous potassium-ion batteries. J Mater Chem A. 2017;5(43):22465.

[71] Huang B, Liu Y, Lu Z, Shen M, Zhou J, Ren J, Li X, Liao S. Prussian Blue $K_2FeFe(CN)_6$ doped with nickel as a superior cathode: an efficient strategy to enhance potassium storage performance. ACS Sustain Chem Eng. 2019;7(19):16659.

[72] Huang B, Shao Y, Liu Y, Lu Z, Lu X, Liao S. Improving potassium-ion batteries by optimizing the composition of prussian blue cathode. ACS Appl Energy Mater. 2019;2(9):6528.

[73] Wessells CD, Peddada SV, Huggins RA, Cui Y. Nickel hexacyanoferrate nanoparticle electrodes for aqueous sodium and potassium ion batteries. Nano Lett. 2011;11(12):5421.

[74] Lee HW, Pasta M, Wang RY, Ruffo R, Cui Y. Effect of the alkali insertion ion on the electrochemical properties of nickel hexacyanoferrate electrodes. Faraday Discuss. 2014;176:69.

[75] Zheng J, Deng W, Hu Z, Zhuo Z, Liu F, Chen H, Lin Y, Yang W, Amine K, Li R, Lu J, Pan F. Asymmetric K/Li-ion battery based on intercalation selectivity. ACS Energy Lett. 2018;3(1): 65.

[76] Deng L, Yang Z, Tan L, Zeng L, Zhu Y, Guo L. Investigation of the Prussian blue analog $Co_3[Co(CN)_6]_2$ as an anode

material for nonaqueous potassium-ion batteries. Adv Mater. 2018;30(31):1802510.

[77] Bie XF, Kubota K, Hosaka T, Chihara K, Komaba S. A novel K-ion battery: hexacyanoferrate(II)/graphite cell. J Mater Chem A. 2017;5(9):4325.

[78] Jiang X, Zhang T, Yang L, Li G, Lee JY. A Fe/Mn-based prussian blue analogue as a K-rich cathode material for potassium-ion batteries. Chemelectrochem. 2017;4(9):2237.

[79] Xue LG, Li YT, Gao HC, Zhou WD, Lu XJ, Kaveevivitchai W, Manthiram A, Goodenough JB. Low-cost high energy potassium cathode. J Am Chem Soc. 2017;139(6):2164.

[80] Luo Y, Shen B, Guo B, Hu L, Xu Q, Zhan R, Zhang Y, Bao S, Xu M. Potassium titanium hexacyanoferrate as a cathode material for potassium-ion batteries. J Phys Chem Solids. 2018; 122:31.

[81] Islas-Vargas C, Guevara-Garcia A, Oliver-Tolentino M, Ramos-Sanchez G, Gonzalez I, Galvan M. Experimental and theoretical investigation on the origin of the high intercalation voltage of $K_2Zn_3[Fe(CN)_6]_2$ cathode. J Electrochem Soc. 2018; 166(3):A5139.

[82] Heo JW, Chae MS, Hyoung J, Hong S-T. Rhombohedral potassium–zinc hexacyanoferrate as a cathode material for nonaqueous potassium-ion batteries. Inorg Chem. 2019;58(5): 3065.

[83] Zhang L, Chen L, Zhou X, Liu Z. Towards high-voltage aqueous metal-ion batteries beyond 1.5 V: the zinc/zinc hexacyanoferrate system. Adv Energy Mater. 2015;5(2):1400930.

[84] Wu X, Jian Z, Li Z, Ji X. Prussian white analogues as promising cathode for non-aqueous potassium-ion batteries. Electrochem Commun. 2017;77:54.

[85] Padigi P, Thiebes J, Swan M, Goncher G, Evans D, Solanki R. Prussian Green: a high rate capacity cathode for potassium ion batteries. Electrochim Acta. 2015;166:32.

[86] He G, Nazar LF. Crystallite size control of prussian white analogues for nonaqueous potassium-ion batteries. ACS Energy Lett. 2017;2(5):1122.

[87] Li C, Wang X, Deng W, Liu C, Chen J, Li R, Xue M. Size engineering and crystallinity control enable high-capacity aqueous potassium-ion storage of prussian white analogues. Chemelectrochem. 2018;5(24):3887.

[88] Sun YP, Xie J, Zhao XB, Zhuang DG, Zhang GL. Prussian blue cathode material: preparation by ion-exchange method and electrochemical potassium-storage performance. Chin J Inorg Chem. 2020;36(1):106.

[89] Husmann S, Zarbin AJG. Cation effect on the structure and properties of hexacyanometallates-based nanocomposites: improving cathode performance in aqueous metal-ions batteries. Electrochim Acta. 2018;283:1339.

[90] Nossol E, Souza VHR, Zarbin AJG. Carbon nanotube/Prussian blue thin films as cathodes for flexible, transparent and ITO--free potassium secondary battery. J Colloid Interface Sci. 2016; 478:107.

[91] Zhu YH, Yin YH, Yang X, Sun T, Wang S, Jiang YS, Yan JM, Zhang XB. Transformation of rusty stainless-steel meshes into stable, low-cost, and binder-free cathodes for high-performance potassium-ion batteries. Angew Chem Int Ed Engl. 2017; 56(27):7881.

[92] Sun Y, Liu C, Xie J, Zhuang D, Zheng W, Zhao X. Potassium manganese hexacyanoferrate/graphene as a high-performance cathode for potassium-ion batteries. New J Chem. 2019;43(29): 11618.

[93] Morant-Giner M, Sanchis-Gual R, Romero J, Alberola A, Garcia-Cruz L, Agouram S, Galbiati M, Padial NM, Waerenborgh JC, Marti-Gastaldo C, Tatay S, Forment-Aliaga A, Coronado E. Prussian Blue@MoS_2 layer composites as highly efficient cathodes for sodium– and potassium-ion batteries. Adv Funct Mater. 2018;28(27):1706125.

[94] Xue L, Li L, Huang Y, Huang R, Wu F, Chen R. Polypyrrole-modified prussian blue cathode material for potassium ion batteries via in situ polymerization coating. ACS Appl Mater Int. 2019;11(25):22339.

[95] Zhang SP, Wang G, Wang BB, Wang JM, Bai JT, Wang H. 3D carbon nanotube network bridged hetero-structured Ni–Fe–S nanocubes toward high-performance lithium, sodium, and potassium storage. Adv Funct Mater 2020:2001592. https://doi.org/10.1002/adfm.202001592.

[96] Chen X, Zeng S, Muheiyati H, Zhai Y, Li C, Ding X, Wang L, Wang D, Xu L, He Y, Qian Y. Double-shelled Ni–Fe–P/N-doped carbon nanobox derived from a prussian blue analogue as an electrode material for K-ion batteries and Li–S batteries. Acs Energy Lett. 2019;4(7):1496.

[97] Wang J, Wang B, Liu X, Bai J, Wang H, Wang G. Prussian blue analogs (PBA) derived porous bimetal (Mn, Fe) selenide with carbon nanotubes as anode materials for sodium and potassium ion batteries. Chem Eng J. 2020;382:1706125.

[98] Stilwell DE, Park KH, Miles MH. Electrochemical studies of the factors influencing the cycle stability of Prussian blue films. J Appl Electrochem. 1992;22(4):325.

[99] Zampardi G, Sokolov SV, Batchelor-McAuley C, Compton RG. Potassium (de-)insertion processes in prussian blue particles: ensemble versus single nanoparticle behaviour. Chem-Eur J. 2017;23(57):14338.

[100] Xiao X, Zhang G, Xu Y, Zhang H, Guo X, Liu Y, Pang H. A new strategy for the controllable growth of MOF@PBA architectures. J Mater Chem A. 2019;7(29):17266.

Yong Liu received his B.Eng. degree from Tianjin University in 2003. Before he received his PhD degree from Tianjin University in 2012, he was a joint Ph.D. student under supervision of Prof. Meilin Liu at Georgia Institute of Technology. He is currently an associate professor of School of Materials Science and Engineering at Henan Univeristy of Science and Technology. His research interests include nanostructured materials and their applications, especially for batteries and electrocatalysis.

Feng-Zhang Ren received Ph.D. degree from Xi'an Jiaotong University. He is currently a distinguished professor of School of Materials Science and Engineering at Henan Univeristiy of Science and Technology. So far, he has published more than 100 SCI papers. His current research is focused on the design and synthesis of novel nanostructured materials and their applications in advanced metallic materials and energy-relating materials.